Rock Mechanics and Rock Engineering (2025) 58:7203–7234
https://doi.org/10.1007/s00603-025-04493-w

ORIGINAL PAPER

Studies on Mechanical Properties and Failure Characteristics of Anisotropic Shale Under True Triaxial Loading at Real-Time High Temperature

Yingjie Xia[1,2,3] · Yusheng Wang[1,2] · Hai Yang[5] · Danchen Zhao[1,2,4] · Zhenyu Yin[4] · Chun'an Tang[1,2] · Jian Chen[5]

Received: 9 June 2024 / Accepted: 24 February 2025 / Published online: 19 March 2025

Abstract

The efficient extraction of deep shale gas (burial depth > 3500 m) in challenging high-temperature and high-stress environments plays a pivotal role in advancing natural gas development. This study investigates how real-time high temperatures and bedding plane inclinations (BPI) affect the mechanical properties of shale, including strength, deformation, and brittleness, under true triaxial loading conditions. Experiments on Longmaxi Formation shale reveal that the true triaxial compressive strength (TCS) and elastic modulus (TEM) exhibit significant temperature thresholds between 120 ℃ and 160 ℃, attributed to the dissipation of adsorbed water in clay minerals speculatively. Failure modes are significantly affected by temperature and bedding plane inclination (BPI). Notably, for samples with a 45° BPI, fracture strike changes occur at higher temperatures (160 ℃ and 200 ℃) due to reduced shear strength along bedding planes. Numerical simulations confirm that this is driven by differing thermal expansion coefficients between bedding planes and the matrix. Additionally, brittleness, evaluated through stress–strain based indices, is affected by temperature, BPI, and loading direction relative to bedding planes. These findings significantly advance the understanding of anisotropic shale behavior under high-temperature conditions, offering insights for optimizing engineering strategies in deep shale gas extraction.

Highlights

- True triaxial compression tests were conducted on shale with varying bedding plane inclinations and temperatures to investigate its mechanical properties.
- The changes of mechanical properties and failure characteristics of anisotropic shale with temperature were obtained and analyzed.
- The anisotropy of mechanical properties of shale at high temperature under true triaxial loading was obtained and analyzed.
- The brittleness of shale, evaluated based on stress–strain curves, is influenced by both temperature and bedding plane inclination, and the relative orientation between the σ_2 loading direction and the strike of the bedding plane significantly affects the brittleness of shale.

Keywords Real-time high temperature · True triaxial compression test · Anisotropy · Shale · Brittleness evaluation

✉ Danchen Zhao
danchen-simon.zhao@connect.polyu.hk

[1] State Key Laboratory of Coastal and Offshore Engineering, Dalian University of Technology, Dalian 116024, China

[2] School of Civil Engineering, Dalian University of Technology, Dalian 116024, China

[3] State Key Laboratory of Geomechanics and Geotechnical Engineering, Institute of Rock and Soil Mechanics, Chinese Academy of Sciences, Wuhan 430071, China

[4] Department of Civil and Environmental Engineering, The Hong Kong Polytechnic University, Hung Hom, Kowloon, Hong Kong, China

[5] CNPC Chuanqing Drilling Engineering Company Limited, Chengdu 610051, China

List of Symbols

BPI	Bedding plane inclination/°
β	Inclination angle of bedding plane/°
RT	Room temperature/℃
σ_1, σ_2,σ_3	Maximum principal stress, intermediate principal stress, minimum principal stress/MPa
$\varepsilon_{\mathrm{p1}}$, $\varepsilon_{\mathrm{p2}}$,$\varepsilon_{\mathrm{p3}}$	Principal strain in the direction of maximum principal stress, intermediate principal stress and minimum principal stress
TCS	Triaxial compressive strength/MPa
TEM	Triaxial elastic modulus/GPa
η	Normalized coefficient of mechanical property
θ	Inclination of fracture/°
B	Brittleness index
B'	Normalized brittleness index
ε_{R}	Pre-peak recoverable strain
E	Elastic modulus/GPa
H	Hardening modulus/GPa
M	Post-peak modulus/GPa
σ_{p}	Peak strength/MPa
σ_{r}	Residual strength/MPa
ε_{r}	Residual strain
$k_{\mathrm{ac(AC)}}$	Slope of the line from the initial yielding point to the residual strength start point
m	Coefficient of heterogeneity
λ	Thermal conductivity coefficient/$(\mathrm{W}/(\mathrm{m}\cdot\mathrm{K}))$
α	Thermal expansion coefficient/$(1/\mathrm{K})$
C	Specific heat capacity/$(\mathrm{J}/(\mathrm{kg}\cdot\mathrm{K}))$
R_C	Anisotropy coefficient
σ_{n}	Normal stress on the bedding plane
τ	Shear stress on the bedding plane
φ	Internal friction angle
c	Cohesion

1 Introduction

Shale gas, as a clean and green non-renewable energy source, is a type of natural gas found within shale formations. The efficient extraction of shale gas to replace traditional fossil fuels is crucial for reducing carbon emissions and achieving carbon neutrality. The Sichuan Basin in China is particularly rich in shale gas reserves, and numerous wells have already been established in this region (Zou et al. 2015; Ma et al. 2020). However, deep shale gas reservoirs, unlike shallower reservoirs (burial depth < 2500 m) or middle-depth reservoirs (2500 m < burial depth < 3500 m), are subject to higher formation temperatures and in situ stresses. For instance, as a representative case, the Lu-202 well in Changning County, Sichuan Province, reaches a vertical depth of over 4500 m with a reservoir temperature exceeding 140 ℃ (Guo et al. 2022b). These conditions significantly alter the mechanical properties of shale, affecting aspects such as permeability, brittleness, and failure mechanisms (Huang et al. 2022). Additionally, the presence of bedding planes in shale induces significant anisotropic variations in mechanical properties and failure characteristics, profoundly impacting the hydro-fracturing process (Guo et al. 2022a; Zhang et al. 2024). Therefore, in the context of deep shale gas development, it is essential to thoroughly investigate the anisotropic effects on the mechanical properties and failure characteristics of shale. This is particularly relevant under conditions involving high true triaxial stress and real-time high temperatures.

In recent years, research on the anisotropy of rock mechanical properties has primarily focused on uniaxial or conventional triaxial tests conducted on rocks with various bedding plane inclinations (BPI) at room temperature. Uniaxial compression tests have revealed that the strength of specimens compressed perpendicular to the bedding plane is significantly higher than that of specimens compressed parallel to the bedding plane (Liu et al. 2023). In conventional triaxial tests, as the angle between the bedding plane and the horizontal plane increases, the peak strength curve exhibits a "U-shaped" pattern with the BPI, with the most unfavorable BPI typically ranging between 45° and 60° (Cheng et al. 2015; Yang et al. 2019; Zhao et al. 2022a, b). Similarly, the tensile strength of shale discs under dynamic Brazilian splitting tests also demonstrates a "U-shaped" variation with increasing BPI (Feng et al. 2022). Saroglou and Tsiambaos (2008) introduced an anisotropy-considerate Hoek–Brown criterion for intact rock, which was further refined by Zhang et al. (2021a) to account for hydration in unsaturated intact anisotropic shale, successfully predicting the strength of anisotropic rock under varying confining pressures. With the growing interest in deep shale gas exploration, the testing of deep shale mechanical properties at high temperatures has gained increasing attention. Han et al. (2023) conducted conventional triaxial tests on shale at real-time temperatures up to 170 ℃, observing a significant influence of temperature on shale's mechanical properties. Guo et al. (2023) performed conventional triaxial tests on shale under different confining pressures at temperatures up to 150 ℃, developing GSI-strength degradation and constitutive models for Longmaxi shale based on the Hoek–Brown criterion using the test data. Studies involving real-time heating uniaxial or triaxial compression tests on shale with BPIs of 0° and 90° indicated that high temperatures alter the anisotropic response of shale's mechanical properties (Masri et al. 2014; Wang et al. 2021), and that high-temperature treatment continues to affect shale's mechanical properties post-treatment (Huang et al. 2022). These studies have confirmed the significant impact of temperature on shale's mechanical properties, yet some have not thoroughly explored the effects of shale anisotropy and were limited by the capabilities of the testing equipment, which were restricted to uniaxial or conventional triaxial tests. Research has shown that the brittleness of rock under true triaxial loading conditions is greater than under conventional triaxial loading conditions (Vachaparampil and Ghassemi 2017; Zhang et al. 2021b; Zheng et al. 2023). Therefore, it is also essential to consider the mechanical properties and failure characteristics of deep shale gas under conditions of high in situ stress and significant horizontal stress differences.

Brittleness is a crucial metric for assessing a rock's fracturing capability. A higher brittleness index indicates a shorter hydraulic fracture length and a higher likelihood of forming complex fracture networks, whereas lower brittleness tends to result in simpler bi-wing fractures (Rickman et al. 2008; Tao et al. 2020). In the context of deep shale gas reservoirs, understanding how the brittleness of anisotropic shale changes at high temperatures is essential. Definitions of brittleness vary: Obert and Duvall (1967) considered materials that fracture at or just above the yield stress as brittle. Andreev (1995) described brittleness as the rock's ability to deform under external forces without undergoing permanent deformation. Goktan and Yilmaz (2005) defined brittle rocks as those that fail under low stress without significant deformation. Rickman et al. (2008) associated brittleness with the elastic modulus and Poisson's ratio, suggesting that a higher elastic modulus and a lower Poisson's ratio indicate greater brittleness. However, under triaxial compression tests, both the elastic modulus and Poisson's ratio increase, contradicting the general trend of decreasing rock brittleness under high confining pressure. This suggests that these measures are only applicable under uniaxial compression conditions (Xia et al. 2017). Hucka and Das (1974) identified several high brittleness phenomena, including low elongation values, fracture failure, fines formation, a high compressive-to-tensile strength ratio, high resilience, a high internal friction angle, and crack formation in indentation. Consequently, there is no unified definition of rock brittleness. To evaluate rock brittleness more accurately, brittleness indices based on stress–strain curves, mineral composition, and parameters from specific tests are often used (Meng et al. 2015; Xia et al. 2019; Zhang et al. 2021b). Geng et al. (2016) evaluated the brittleness of Longmaxi Formation shale under conventional triaxial test conditions using five brittleness indices based on the stress–strain curve, finding that the anisotropy of shale brittleness decreased with increasing confining pressure for certain BPIs. Zhao et al. (2023c) discovered that while the anisotropy of strength and deformation parameters of shale closely correlated with the content of quartz and clay minerals, brittleness anisotropy did not. Guo et al. (2020; 2022b) heated Longmaxi Formation shale samples from the Sichuan Basin with BPIs of 0°, 30°, 45°, 60°, and 90°, conducting uniaxial compression tests after cooling to room temperature under both natural and flowing water conditions. Their findings indicated that heating treatment significantly affects shale brittleness.

In summary, to investigate the anisotropic variations in the mechanical properties and failure characteristics of shale under the high temperature and high in situ stress environment of deep shale gas reservoirs, this study conducted true triaxial tests and numerical simulations on Longmaxi Formation shale. The bedding planes of the shale samples intersected the horizontal plane at angles of 0°, 30°, 45°, 60°, and 90°. The temperatures during the tests were maintained at room temperature (RT), 80 ℃, 120 ℃, 160 ℃, and 200 ℃. We obtained the stress–strain curves and failure modes, exploring the mechanisms by which temperature and bedding plane inclination (BPI) influence shale failure modes. Furthermore, we quantitatively evaluated the variation in shale brittleness under different testing conditions and determined the impact of real-time high temperature on the anisotropy of shale's mechanical properties and failure characteristics. This research provides valuable insights into the anisotropy laws of shale and offers important guidance for deep shale gas exploitation projects.

2 Experimental Methodologies

2.1 Sample Preparation

The samples used in this experiment, which are representative of deep shale gas reservoirs, were sourced from the outcrops of the Longmaxi Formation shale in the Wulong area of the Sichuan Basin, China (Fig. 1). Following the guidelines recommended by the International Society for Rock Mechanics (ISRM) (Fairhurst and Hudson 1999), intact portions of the rock mass were fashioned into cuboid specimens measuring 50 mm × 50 mm × 100 mm, ensuring that the non-uniformity and non-perpendicularity of the samples were less than 0.02 mm. To investigate the anisotropy of shale, samples with five different bedding plane inclinations (BPI) of 0°, 30°, 45°, 60°, and 90° were prepared along various bedding plane orientations during the cutting process, as depicted in Fig. 1b. As illustrated in Fig. 2a, the black shales feature several layers of earth-yellow bedding planes, which are macroscopically visible pyrite bedding planes characteristic of the Longmaxi Formation shale (Chen and Jin 2012; Rybacki et al. 2016). In the Longmaxi Formation shale from the southern Sichuan Basin, the approximate content of clay minerals is 35.35%, quartz minerals 35.08%, feldspar minerals 6.48%, calcite minerals 13.66%, and pyrite 3.18% (Guo et al. 2022c).

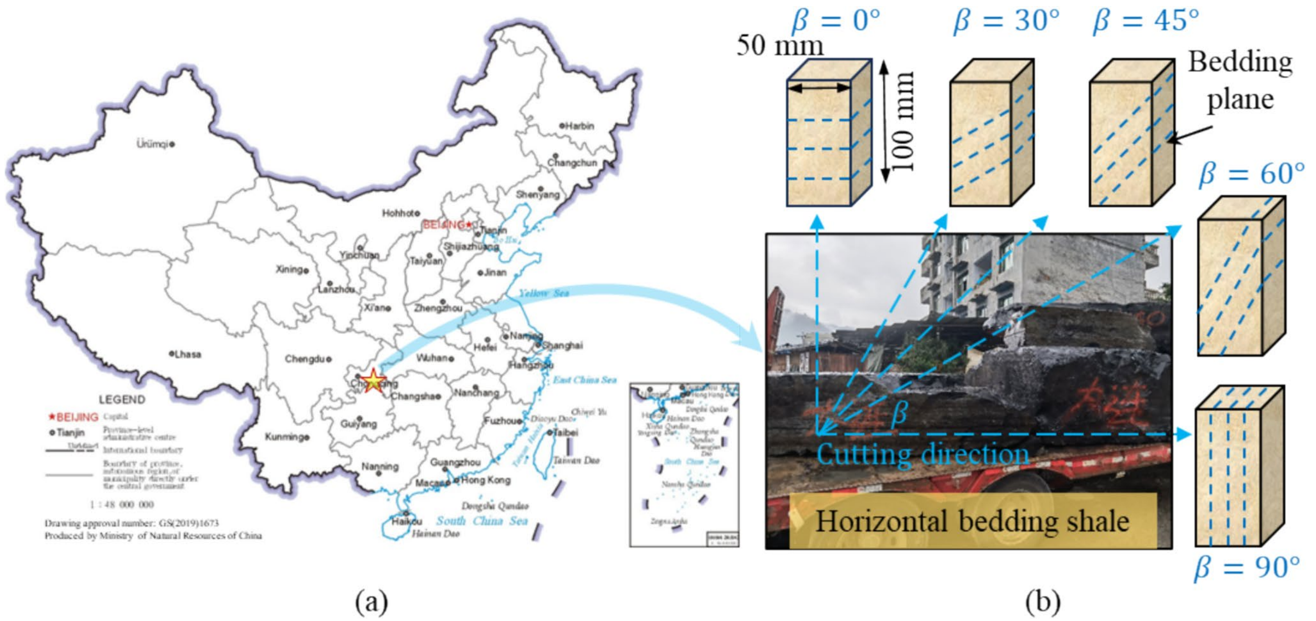

Fig. 1 Location of the shale (**a**), and schematic diagram of shale samples with five different BPIs in this study (**b**)

2.2 Testing Apparatus

The testing apparatus utilized was the real-time high-temperature true triaxial test equipment, a collaborative development by the Wuhan Institute of Rock and Soil Mechanics of the Chinese Academy of Sciences and Qingdao University of Technology, as depicted in Fig. 2d. This equipment consists of a rigid loading frame, a hydraulic pump system, a temperature control system, and a test operation and data monitoring system. The temperature control system is capable of independently managing the activation and deactivation of heaters in contact with the four horizontal faces of the sample, as well as regulating the target temperature and heating rate. Each of the four horizontal loading plates is equipped with nine rigid electric heaters, totaling 36, and a thermocouple is embedded in each plate to monitor the temperature, providing real-time feedback on the temperature of the rock specimen's surfaces in direct contact with the plates. The advanced heating system is capable of heating the surface of the rock specimen to a maximum of 600℃, ensuring precise temperature control critical for high-temperature experiments. The test operation and data monitoring system can independently apply the desired stress in the three principal stress directions, control the rate of stress increase, and record the data. The equipment employs linear variable differential transformers (LVDTs) to measure displacement in the three principal stress directions. Figure 2e illustrates the internal loading chamber with the sample installed. For a cuboid rock specimen measuring 50 mm × 50 mm × 100 mm, the device can apply a maximum stress of 1000 MPa in the vertical direction (σ_1) and 200 MPa in both the forward and lateral directions (σ_2 and σ_3). Further details about the test equipment are available in the paper by Ma et al. (2023).

2.3 Testing Procedure

The testing protocol is outlined in Table 1. The angles between the bedding plane and the horizontal plane were set at 0°, 30°, 45°, 60°, and 90° (Fig. 2a). Real-time temperatures were established at room temperature (RT), 80 ℃, 120 ℃, 160 ℃, and 200 ℃, based on the temperature of deep shale gas reservoirs (Guo et al. 2020; Zhou et al. 2024). This selection also considered the observation that Longmaxi Formation shale undergoes macroscopic failure when heated beyond 220 ℃ (Guo et al. 2020), resulting in a total of 25 shale samples being tested. The confining pressures σ_2 and σ_3 were set at 80 MPa and 60 MPa, respectively, to simulate the high in situ stress and the differential horizontal stress present in deep shale gas formations (Nie et al. 2023; Zhou et al. 2024). The direction of stress loading is depicted in Fig. 2c, with the strike of the bedding plane perpendicular to the σ_2 direction. To facilitate fracture identification, the surface of the rock sample with an inclined bedding plane is labeled as Surface 1, and the sides of the rock specimen are numbered 1–4 in a counterclockwise direction. Surfaces 1 and 3 correspond to the σ_2 direction, while Surfaces 2 and 4 correspond to the σ_3 direction. Prior to testing, the samples underwent anti-friction treatment (as illustrated in Fig. 2b). Each side of the sample was tightly sandwiched between two layers of 0.05 mm thick copper sheets, with high-temperature lubricant evenly applied between the sheets to minimize end effects. It is important to note that although only one test

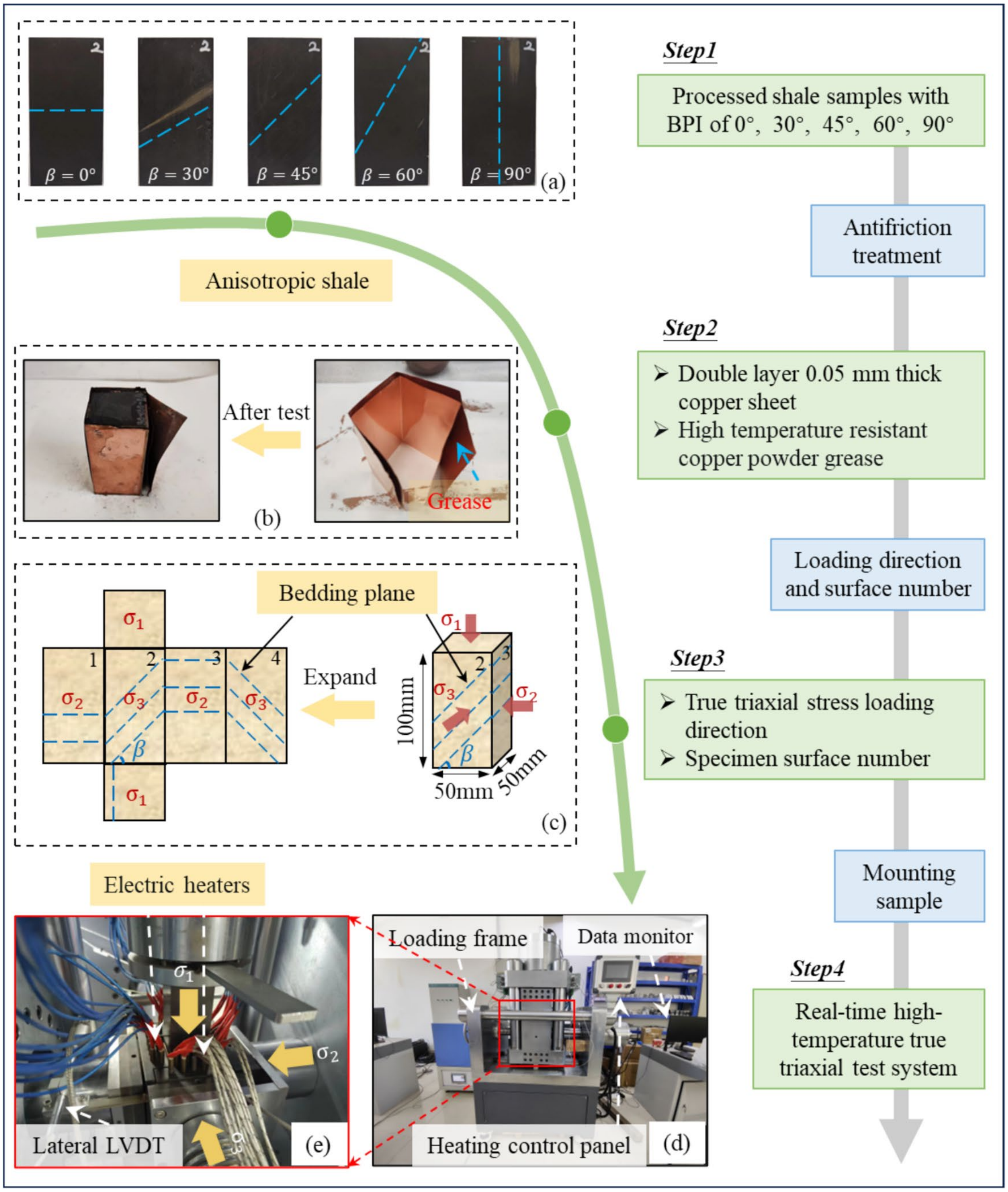

Fig. 2 Shale samples with five different BPIs (**a**), antifriction treatment before the test (**b**), schematic diagram of principal stress loading direction (**c**), real-time high-temperature true triaxial testing system used in this study (**d**), loading chamber (**e**)

was conducted for each condition, the results obtained were clear and consistent with those from other relevant true triaxial tests (Vachaparampil and Ghassemi 2017; Zhang et al. 2021b; Ma et al. 2023).

Table 1 Test conditions

BPI/°	Temperature/℃	σ_2/MPa	σ_3/MPa
0	RT, 80, 120, 160, 200	80	60
30			
45			
60			
90			

Figure 3 illustrates the stress and temperature loading path for the test condition at 200 ℃. Initially, hydrostatic pressure was applied at a rate of 6 MPa/min until all three principal stresses reached 60 MPa. Once the hydrostatic pressure was attained, the rock sample was heated to 200 ℃ at a rate of 5 ℃/min. After reaching the target temperature,

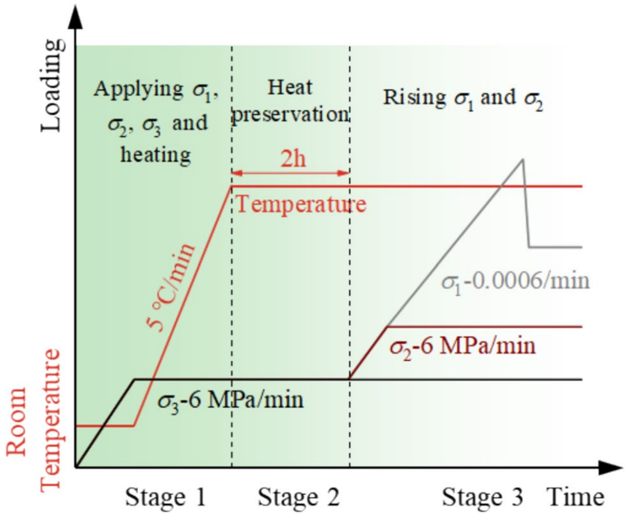

Fig. 3 Stress and temperature loading path and loading rate

the sample was maintained at this temperature for 2 h to ensure uniform internal heating, which can better reduce the temperature disturbance of the shale samples (Ma et al. 2023). Subsequently, σ_2 and σ_3 were synchronously increased to the target stress of 80 MPa at a rate of 6 MPa/min. Thereafter, the control mode for σ_1 was switched to a strain loading rate of 0.0006/min until the sample failed. Meanwhile, σ_2 and σ_3 were maintained at 80 MPa and 60 MPa, respectively, and the temperature was kept constant at 200℃ until the completion of the test.

3 Experimental Results

3.1 Stress–Strain Curves

Figure 4 illustrates the stress–strain curves of shale samples with varying bedding plane inclinations (BPI) at room temperature (RT), 80 ℃, 120 ℃, 160 ℃, and 200 ℃. These curves generally exhibit four distinct stages: pore and crack compaction, elastic deformation, unstable fracture development, and residual deformation. The pore and crack compaction stage is less pronounced in the stress–strain curves due to the compaction effect of high hydrostatic pressure on the shale's pores and cracks. Examining the stress–strain curves at different temperatures, it is evident that the elastic modulus and peak strength of shale samples with different BPIs vary significantly, highlighting the anisotropy in shale's mechanical properties. The peak strains in the σ_2 and σ_3 directions show that in true triaxial tests of isotropic rock, the presence of σ_2 usually restricts deformation in this direction, leading to more significant deformation in the σ_3 direction. When the bedding plane orientation is parallel to the σ_3 direction, the difference between σ_2 and σ_3 strains decrease. In some cases, such as shale samples with a BPI of 45° at 200 ℃, the σ_2 strain may even exceed the σ_3 strain. This indicates that the bedding plane influences the anisotropy of deformation caused by σ_2 in true triaxial tests. All stress–strain curves exhibit a negative post-peak modulus, characteristic of Class I rock behavior. After the peak, energy absorption is necessary for continued failure, leading to some plastic deformation behaviors in shale (Wawersik and Fairhurst 1970; Wang et al. 2020b). Some samples experience stress drops after peak strength, indicating matched brittle fracture processes rather than sudden uncontrollable stress drops (Zheng et al. 2023). In the residual stage, the curves of shale samples with all BPIs at RT and 80 ℃ are stable, whereas samples with BPIs of 30°, 45°, and 60° at 120 ℃ exhibit slight stick–slip behavior. Samples with BPIs of 0°, 45°, 60° at 160 ℃, and 0° and 90° at 200 ℃ show more pronounced stick–slip behavior. This suggests that higher temperatures increase the likelihood of significant stick–slip behavior in the residual stage.

The volumetric strain curves of shale samples with different BPIs at RT, 80 ℃, 120 ℃, 160 ℃, and 200 ℃ show that an increase in volumetric strain indicates compression, while a decrease indicates expansion. Under high confining pressure, most samples contract before reaching peak stress. After peak stress, crack penetration leads to sample failure and volume expansion. However, some samples transition from compression to expansion before peak stress, such as those with a BPI of 30° at RT and 200 ℃. As seen in Fig. 4b and d, the volumetric strain curves before the corresponding peak points at RT and 80 ℃ exhibit an upward concave shape with gradually increasing slopes. The curves are relatively dispersed at lower temperatures, reflecting shale's anisotropy. At 120 ℃ (Fig. 4f), the front part of the curves before the peak point shows an upward concave trend with a gradual slope increase, and the middle and later stages are almost linear. This trend becomes more pronounced at 160 ℃ and 200 ℃ (Fig. 4h and j). Moreover, the curves at 120 ℃, 160 ℃, and 200 ℃ are more clustered than those at RT and 80℃, suggesting that higher temperatures may reduce shale's anisotropy.

3.2 Mechanical Properties

The compressive strength and elastic modulus are fundamental parameters for evaluating the failure bearing capacity and deformation characteristics of rock, providing critical insights into its mechanical behavior. The maximum deviational stress from the true triaxial stress–strain curve was defined as the true triaxial compressive strength (TCS), and the slope between the points corresponding to 30% and 50%

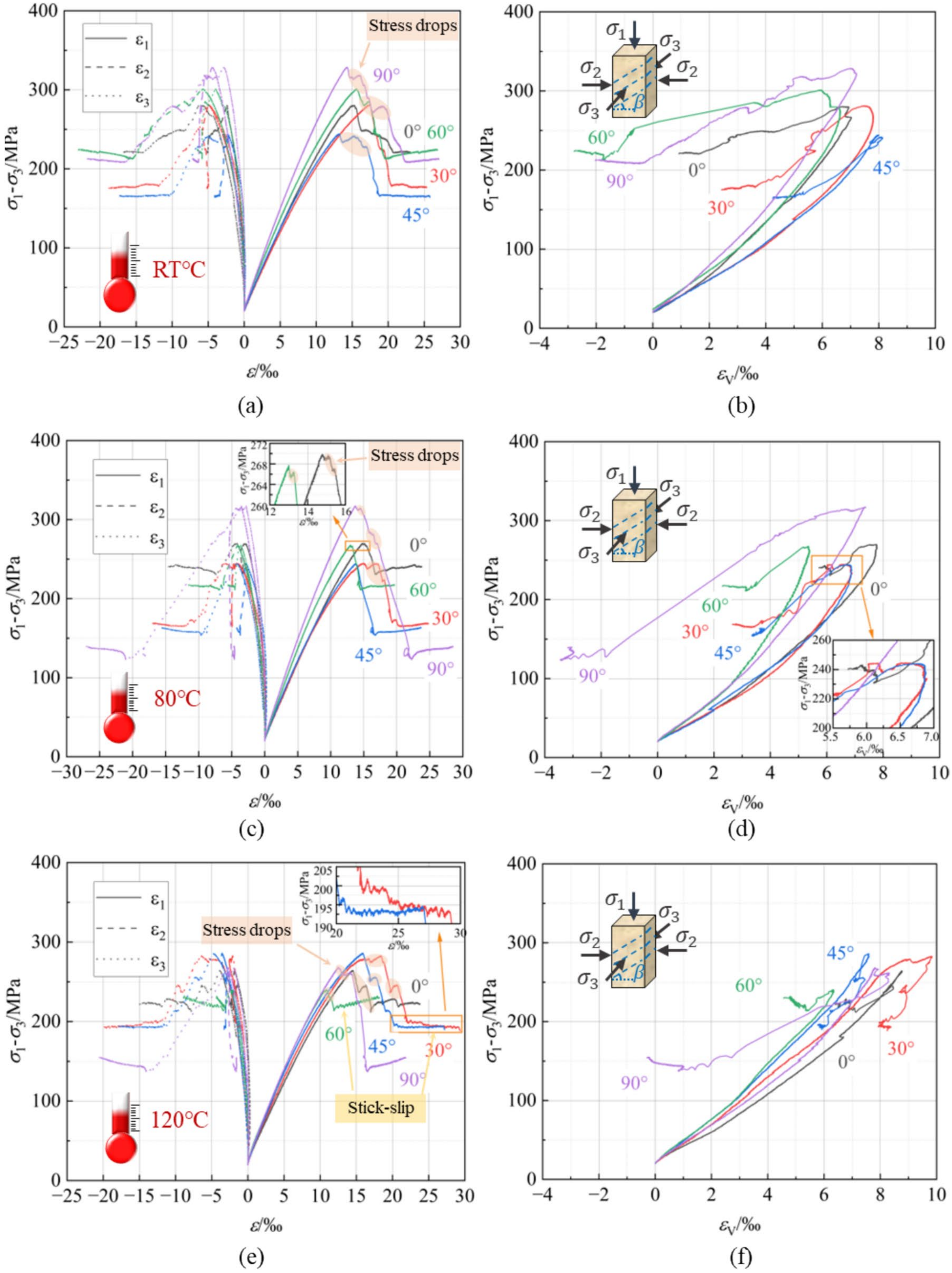

(a) (b)

(c) (d)

(e) (f)

Fig. 4 Stress–strain curves of shales with BPIs of 0°, 30°, 45°, 60°, 90° at RT (**a**) and (**b**), 80 ℃ (**c**) and (**d**), 120 ℃ (**e**) and (**f**), 160 ℃ (**g**) and (**h**), 200 ℃ (**i**) and (**j**)

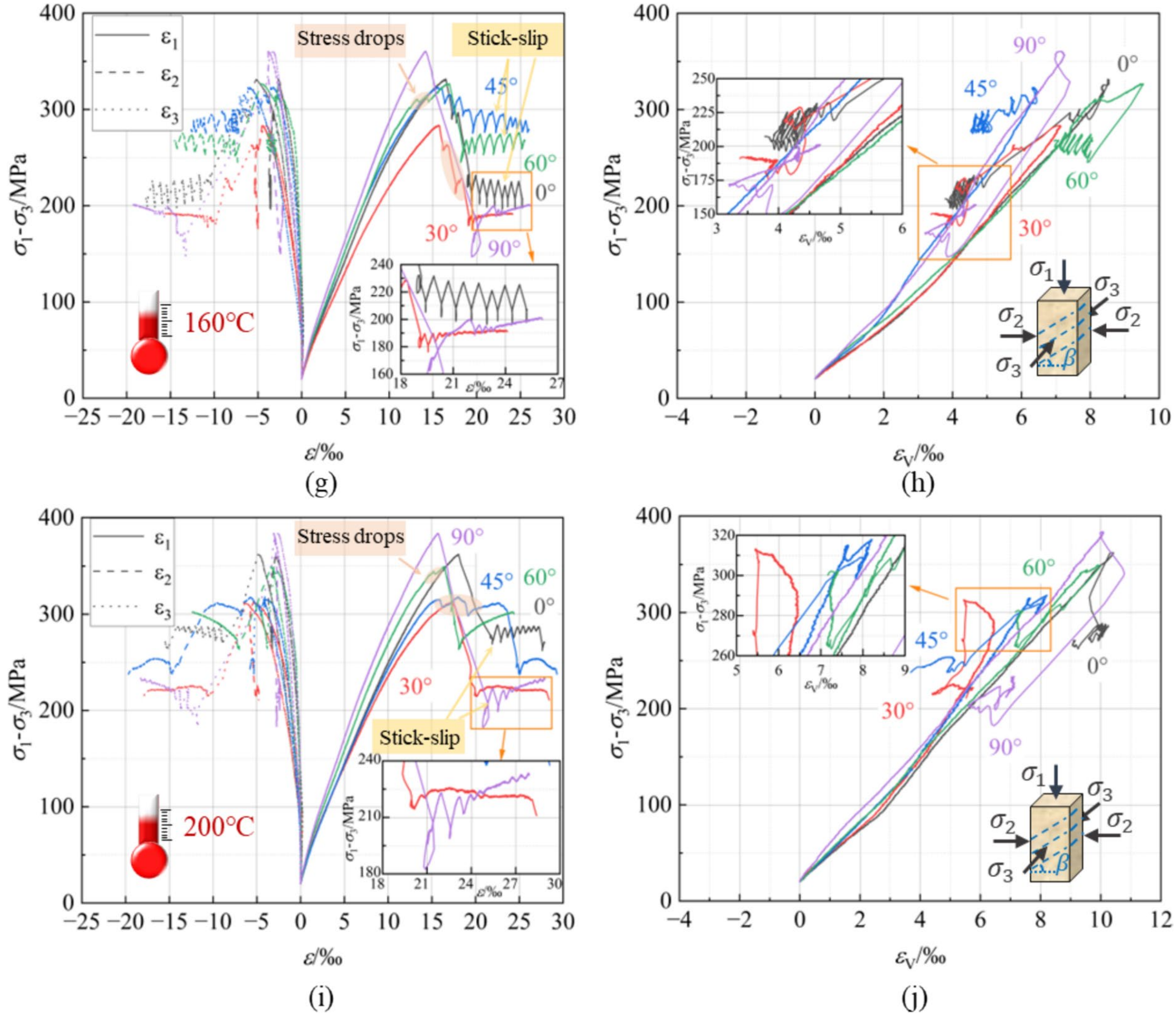

Fig. 4 (continued)

of the TCS values on the curve in the σ_1 direction was identified as the true triaxial elastic modulus (TEM).

As depicted in Fig. 5a, the TCS of shale samples with different BPIs exhibits varying trends with temperature increase. Samples with BPIs of 0°, 60°, and 90° show a

Fig. 5 Evolution of TCS (**a**) and TEM (**b**) with temperature in shales with different BPIs

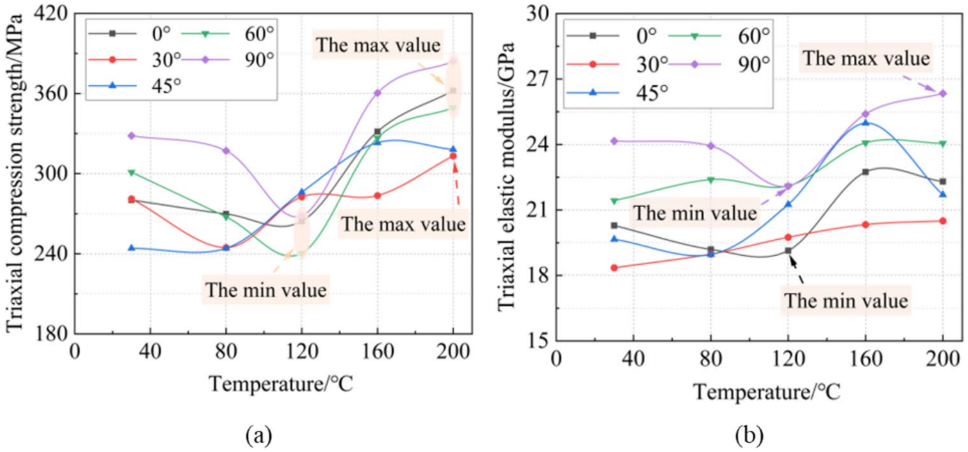

decrease followed by an increase in TCS with temperature, reaching their minimum values at 120 ℃. The maximum TCS values for samples with BPIs of 0°, 60°, and 90° occur at 200 ℃. This suggests a temperature threshold around 120℃ that significantly influences the TCS of shale. As shown in Fig. 5a, shale with a BPI of 30° also exhibits a pattern of decreasing then increasing TCS with temperature. The TCS of shale with a BPI of 45° shows a significant increase at 120 ℃. Figure 5b displays the TEM variations of shale samples with different BPIs with temperature. The TEM curves for shale samples generally exhibit a downward trend followed by an upward recovery as temperature increases, with the lowest TEM values observed in the range of 80–120 ℃. In summary, a temperature threshold near 120 ℃ markedly alters the mechanical property trends of most shale samples, affecting both TCS and TEM.

Figure 6a and b depicts the variation curves of TCS and TEM for shale with BPI at different temperatures. At room temperature, both TCS and TEM curves exhibit a concave shape, with minimum values appearing at BPIs of 30° or 45°, indicating the most pronounced anisotropy at these inclinations. This contrasts with the minimum value under uniaxial compression, which occurs when the angle between the minimum principal stress and the bedding plane is 45°–60° at RT (Saroglou and Tsiambaos 2008; Guo et al. 2022b), due to the anisotropy of deformation caused by the high horizontal stress difference in true triaxial conditions affecting the bedding plane's anisotropy. Figure 7 demonstrates that the distribution of fractures in shale samples with different BPIs also differs significantly from that under uniaxial conditions, confirming that true triaxial loading causes noticeable differences in anisotropy compared to uniaxial compression. With temperature increase, the overall TCS and TEM of shale samples rise. Except at 120℃, with the minimum TCS value at 60° and the minimum TEM value at 0°, the analysis is detailed in the discussion section. In summary, the lowest mechanical properties of shale samples across different temperatures are predominantly observed within the BPI range of 30°–45°, underscoring the critical role of inclination in anisotropic behavior.

Overall, from RT to 200 ℃, shale exhibits a temperature threshold at around 120 ℃. Before this threshold, the TCS of shale remains relatively unchanged or decreases with temperature increase. Beyond the temperature threshold, the TCS of all shale samples with different BPIs shows a marked increase, driven by the dissipation of bound water and enhanced intergranular contact. The impact of temperature on rock failure mechanics is attributed to the competition between temperature strengthening and weakening effects. The former results from intergranular contact compaction due to the volume expansion of certain minerals at high temperatures, while the latter arises from intergranular cracking caused by uneven thermal expansion of different minerals (Ma et al. 2023). Additionally, the improvement or deterioration of rock mechanical properties also depends on the role played by water evaporation and microcracks (Rao et al. 2007). Therefore, the slight reduction in TCS before the temperature threshold may be due to high confining pressure compacting the pores and cracks before axial compression, and the heating treatment leading to uneven thermal expansion of mineral particles, resulting in thermal stress and microcracks (Sun et al. 2015). Thermal stress can also expand existing cracks, causing irreversible damage to the rock structure (Tian et al. 2012). After the temperature threshold, the increase in TCS of shale may be attributed to the dissipation of bound water above 100 ℃ (Guo et al. 2020), which mitigates the degradation of TCS by thermal cracks and significantly improves the TCS of shale.

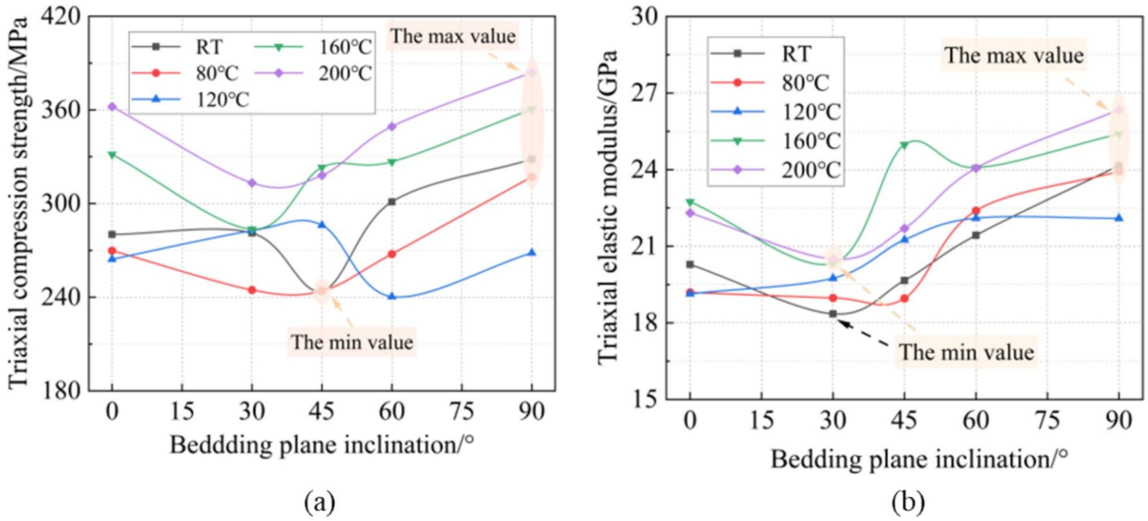

Fig. 6 Evolution of TCS (**a**) and TEM (**b**) of shales with BPIs at different temperatures

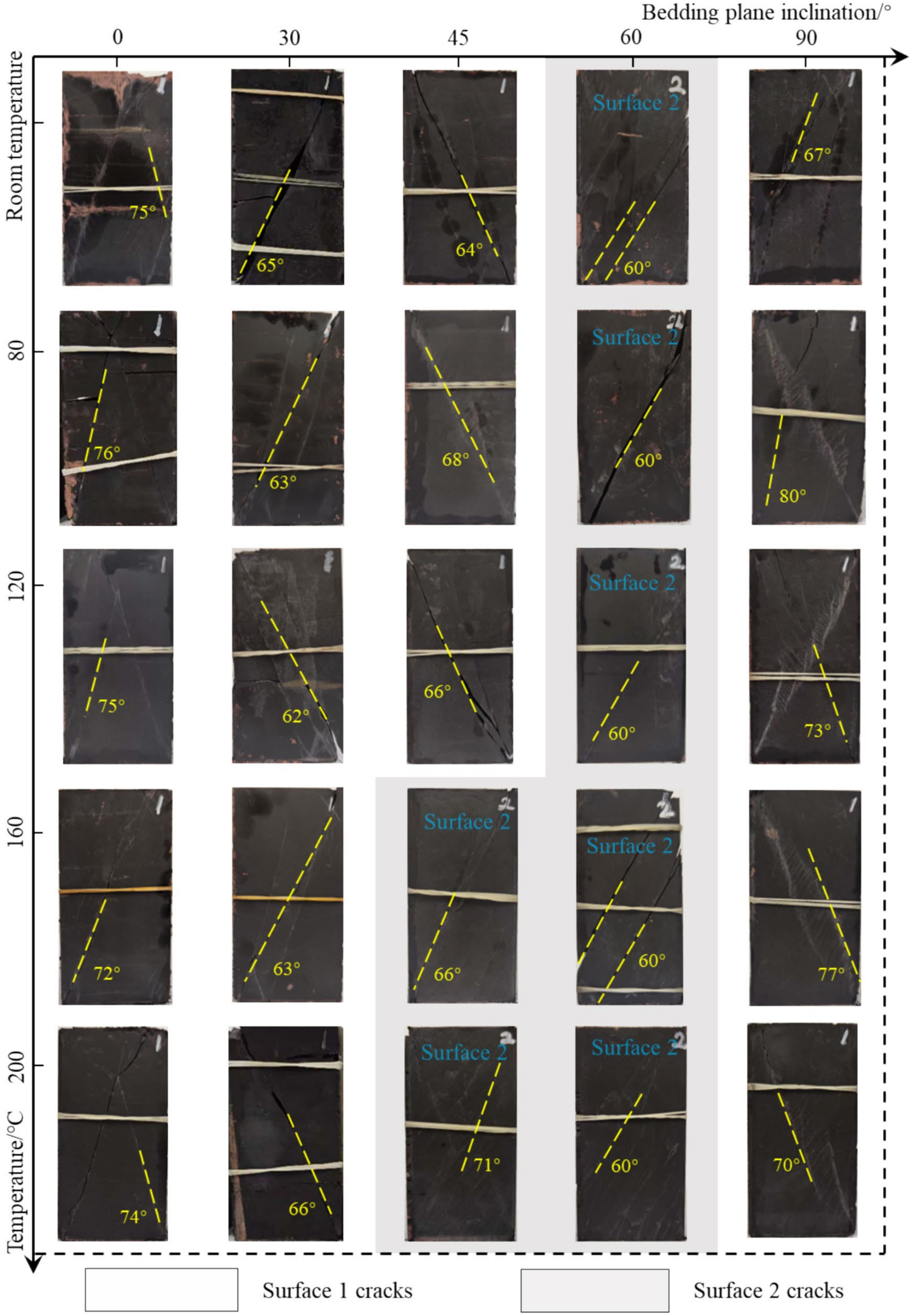

Fig. 7 Failure morphologies of shales under all BPIs and temperatures ranging from RT to 200℃

3.3 Failure Modes

This section explores the failure mechanisms of anisotropic shale by analyzing the failure modes and fracture inclinations under various temperature conditions. Figure 7 presents the fracture morphologies of anisotropic shale samples at room temperature (RT), 80 ℃, 120 ℃, 160 ℃, and 200 ℃. To determine the shale's failure mode, the angle between the fracture plane and the horizontal plane, denoted as the fracture inclination θ, is measured. The failure mode is classified based on θ_{max}: when θ_{max} exceeds 80°, it indicates tensile failure; when θ_{max} exceeds 80° and is accompanied by shear fracture, it signifies tensile-shear composite failure; and when θ_{max} is less than 80°, it represents shear failure (Ma et al. 2023). The majority of the shale samples exhibit fracture planes that are perpendicular to surface 1 and surface 3, and parallel to the σ_2 direction. Under true triaxial loading, σ_2 suppresses microcrack formation, while tensile stress at microcrack tips in the σ_3 direction promotes crack propagation, resulting in fracture planes parallel to σ_2. These findings align with the failure phenomena observed in true triaxial tests (Vachaparampil and Ghassemi 2017; Ma et al. 2023).

The failure mode of anisotropic shale under the influence of temperature shows different results. The fractures of shale samples with a Bedding Plane Inclination (BPI) of 0° display an inverted "V-shape" or a single-slope shear fracture at all temperatures. Two fractures extend upward from the two corners of the bottom edge of surface 1 to the middle and upper part of surface 1. From the junction point, one or two fractures with a more moderate inclination extend to the upper boundary of surface 1. The maximum fracture angle (θ_{max}) is 75°, 76°, 75°, 72°, and 74°, respectively, indicating shear failure. At all temperatures, the fracture morphologies of shale samples with a BPI of 30° almost present diagonal shear fractures distributed on surface 1 and surface 3. The θ_{max} is 65°, 63°, 62°, 63°, and 66°, respectively, all indicating shear failure. For shale with a BPI of 90° at RT, a fracture extends from the lower left corner of surface 1 to the upper boundary, while another fracture is distributed nearly parallel to the right side of the initial fracture with a θ_{max} of 67°, indicating shear failure. At 80 °C and 120 °C, a fracture runs through the top boundary of the sample from the lower corner of surface 1 and presents a cross distribution with this fracture. It consists of several small fracture groups with less inclination than the main fracture, running parallel from the lower corner of surface 1 to the upper corner, intersecting with the main fracture of surface 1. The θ_{max} is 80° and 73°, indicating a tensile-shear composite failure and shear failure. At 160 °C and 200 °C, two fractures in shale samples with a BPI of 90° extend from two corner points in the diagonal direction of surface 1 but do not converge. They are connected by many parallel small fracture groups with opposite tendencies at the middle ends of the two extended fractures. The θ_{max} is 77° and 70°, respectively, indicating shear failure. At RT, 80 °C, and 120 °C, the fracture planes of shale samples with a BPI of 45° are perpendicular to surface 1 and surface 3, with an obvious penetrating fracture roughly distributed along a diagonal. The θ_{max} is 64°, 68°, and 66°, respectively, indicating shear failure. However, at 160 °C and 200 °C, the fracture planes are perpendicular to surface 2 and surface 4 and parallel to the σ_3 direction, presenting a result inconsistent with the failure mode under true triaxial loading. At 160 °C, shale with a BPI of 45° has a penetrating fracture distributed along the diagonal, and at 200 °C, the fractures are generally distributed in two patterns. One fracture extends diagonally from the upper right corner of surface 2 to the lower boundary, and the other extends downward from the upper left corner of surface 2 to intersect it, with θ_{max} of 66° and 71°, respectively, indicating shear failure. The fracture planes of shale samples with a BPI of 60° at all temperatures are perpendicular to surface 2 and surface 4, parallel to the σ_3 direction, with fracture inclinations of 60°, indicating that shear failure occurs along the bedding planes of shale samples with a BPI of 60°.

In summary, the influence of temperature on shale failure mode is closely related to the distribution of the bedding plane. When BPIs are 0°, 30°, 60° and 90°, temperature has little obvious influence on the failure mode of shale. When BPI is 45°, the direction of the fracture plane changes at higher temperatures of 160 °C and 200 °C. Temperature can affect the failure mode of shale samples with certain BPIs under true triaxial loading. Regarding the influence of anisotropy of shale on failure mode at different temperatures, at room temperature (RT), 80 °C, and 120 °C, the shale samples generally show shear failure. The fracture planes of shale samples with a BPI of 60° are parallel to σ_3, whereas the fracture planes of shale samples with other BPIs are parallel to σ_2. At 160 °C and 200 °C, shale samples with all BPIs exhibit shear failure. Specifically, the fracture planes of shale samples with BPIs of 45° and 60° are parallel to σ_3, while those with other BPIs are parallel to σ_2. Shale samples with BPIs of 0° and 90° generally exhibit the highest fracture inclinations. In contrast, samples with a BPI of 60° show shear failure along the bedding plane, resulting in the lowest fracture inclinations. The failure mode of shale results from the combined effects of BPI and temperature.

4 Brittleness Evaluation

4.1 Brittleness Indices Selection

Brittleness indices derived from stress–strain curves are commonly classified into four categories: pre-peak stage, post-peak stage, combined pre- and post-peak stages, and strain energy-based calculations. Mineral composition-based indices assess rock brittleness by quantifying the proportion of brittle minerals within the rock; however, they fail to incorporate external factors such as stress and temperature. Additional brittleness indices are derived from specialized test parameters, including hardness, impact, indentation, and hydraulic fracturing tests, which provide valuable insights into specific rock behaviors. Certain tests, although insightful, involve complex procedures, and their accuracy and reliability under varying geological conditions still require further validation. Given the advantages and limitations of various brittleness indices, this study focuses on those derived from stress–strain curves. These indices were selected to evaluate the brittleness of anisotropic shale under real-time temperature conditions, leveraging the mechanical parameters obtained from the tests. Table 2 provides a comprehensive overview of the brittleness indices employed in this study, detailing their calculation methods and the underlying mechanical parameters. The selected indices are based on stress, strain parameters, and pre-peak and post-peak characteristics for comprehensive evaluation. B_1 calculates the brittleness index using the ratio of pre-peak recoverable strain to peak strain, ranging from 0 to 1. A value of 1 indicates extreme brittleness (Hucka and Das 1974). B_2 uses the ratio of the hardening modulus to the elastic modulus, with the index also ranging from 0 to 1, where 1 signifies extreme brittleness (Rybacki et al. 2016). The hardening modulus is calculated from the slope of the points corresponding to 50% and 100% of the peak strength. B_3 calculates the brittleness index by the ratio of post-peak rupture energy to withdrawn elastic energy, ranging from 0 to + ∞. An index of 0 represents extreme brittleness (Tarasov and Potvin 2013). Among them, the post-peak modulus is calculated from the slope of the corresponding point of the peak strength and the first point of the residual strength. B_4 uses the ratio of post-peak stress drop to peak stress, with the index ranging from 0 to 1, where 1 indicates extreme brittleness (Rybacki et al. 2016). The residual strength is selected from the lowest value reached for the first time after the peak. B_5 considers both the ratio of post-peak stress drop to peak stress and the velocity of the post-peak stress drop, with the index ranging from 0 to 1, and 1 representing extreme brittleness (Meng et al. 2015). B_6 accounts for the rate of post-peak stress drop and the ratio of elastic energy released by failure to the total energy stored at the peak, with the brittleness index ranging from 0 to + ∞. A higher brittleness index indicates higher rock brittleness (Xia et al. 2017).

4.2 Anisotropic Characteristics of Shale Brittleness at Real-Time Temperatures

Table 3 presents the true triaxial test data of anisotropic shale samples at different temperatures. In the test conditions, the first digit represents the test temperature, and the second digit represents the BPI. The calculated brittleness indices $B_1 - B_6$ are shown in Table 4. To facilitate the comparison of the evaluation results of different brittleness indices, the indices are normalized according to Eq. (1):

$$B' = \frac{(B - B_{\min})}{(B_{\max} - B_{\min})} \tag{1}$$

where B' is the normalized brittleness index, $B_{\min}$ and $B_{\max}$ are the minimum and maximum values of the brittleness index under all test conditions. The normalized indices $B'_1 - B'_6$ are shown in Table 4. Since B_3 is negatively correlated with the brittleness of rock, it is treated reciprocally before normalization. The contour plots of $B'_1 - B'_6$ for shale samples with different temperatures and BPIs are shown in Fig. 8a–f, with red representing regions with higher brittleness and blue representing regions with lower brittleness. To explore the consistency of the evaluation results of brittleness indices, a correlation analysis was conducted on the results of $B_1 - B_6$ using the Kendall τ-b method (Zhou and Ma 2024). The calculated Kendall's correlation coefficients among each normalized brittleness index are shown in Fig. 9. When the significance value is less than 0.05, it

Table 2 Selected brittleness indices

Calculation formula	Formula characteristics	Author's conditions of use
$B_1 = \varepsilon_{\mathrm{R}} / \varepsilon_1$	Pre-peak parameters	Rock type: Skarn, Siltstone Test type: Conventional triaxial test
$B_2 = H / E$	Pre-peak parameters	Rock type: Shale Test type: Conventional triaxial test
$B_3 = (M - E) / M$	Post-peak energy ratio B_3 is negatively correlated with brittleness	Rock type: Class I and Class II rock Test type: Conventional triaxial test
$B_4 = \left(\sigma_{\mathrm{p}} - \sigma_{\mathrm{r}}\right) / \sigma_{\mathrm{p}}$	Post-peak parameters	
$B_5 = \frac{\sigma_{\mathrm{p}} - \sigma_{\mathrm{r}}}{\sigma_{\mathrm{p}}} \cdot \frac{\lg\left\lvert k_{\mathrm{ac(AC)}} \right\rvert}{10}$	Post-peak parameters	Rock type: Cement mortar, Marble, Granite Test type: Conventional triaxial test
$B_6 = \frac{\sigma_{\mathrm{p}} - \sigma_{\mathrm{r}}}{\varepsilon_{\mathrm{r}} - \varepsilon_{\mathrm{p}}} + \frac{(\sigma_{\mathrm{p}} - \sigma_{\mathrm{r}})(\varepsilon_{\mathrm{r}} - \varepsilon_{\mathrm{p}})}{\sigma_{\mathrm{p}} \varepsilon_{\mathrm{p}}}$	Post-peak parameters and energy ratio	Rock type: Sandstone Test type: Conventional triaxial test

Table 3 True triaxial experimental data of shale samples

Test condition	σ_p/MPa	$\varepsilon_1/10^{-3}$	σ_r/MPa	$\varepsilon_r/10^{-3}$	$\varepsilon_R/10^{-3}$	H/GPa	E/GPa	M/GPa	$k_{ac(AC)}$
RT-0	280.22	15.17	220.80	20.90	12.83	14.88	20.29	– 10.38	– 10.38
80–0	269.88	14.79	231.94	16.98	13.02	15.02	19.19	– 17.30	– 17.30
120–0	264.37	14.48	219.97	20.73	12.77	14.69	19.14	– 7.11	– 7.11
160–0	331.53	16.45	206.20	19.42	13.70	15.75	22.74	– 42.30	– 42.30
200–0	362.10	18.04	269.15	21.90	15.34	15.86	22.31	– 24.11	– 24.11
RT-30	281.13	17.45	178.37	20.44	14.23	12.47	18.35	– 34.44	– 34.44
80–30	244.69	14.92	165.27	20.34	11.93	12.51	18.84	– 14.65	– 14.65
120–30	282.64	18.39	198.19	22.20	13.30	11.08	19.75	– 22.18	– 11.44
160–30	283.58	15.66	180.28	19.14	12.96	13.91	20.33	– 29.75	– 29.75
200–30	313.21	17.32	216.58	20.00	14.30	13.55	20.50	– 36.10	– 36.10
RT-45	244.09	13.18	167.18	19.44	11.40	14.68	19.66	– 12.28	– 12.28
80–45	244.12	13.77	155.31	16.48	11.82	13.93	18.96	– 32.72	– 32.72
120–45	286.14	15.91	194.70	20.73	12.52	13.56	21.25	– 18.96	– 18.96
160–45	323.16	15.55	277.12	19.60	12.14	15.75	24.98	– 11.37	– 11.37
200–45	318.04	18.00	238.96	25.02	13.74	12.92	21.70	– 11.27	– 7.45
RT-60	301.06	15.59	213.05	19.91	13.11	15.18	21.43	– 20.39	– 20.39
80–60	267.70	13.00	211.39	14.53	11.06	16.41	22.40	– 36.85	– 36.85
120–60	240.40	10.88	213.79	11.90	9.97	17.65	22.10	– 25.96	– 17.12
160–60	326.74	16.88	247.72	18.20	12.74	14.25	24.08	– 60.14	– 12.57
200–60	349.32	16.30	266.23	18.14	13.69	16.46	24.06	– 45.04	– 26.49
RT-90	328.40	14.29	208.72	22.76	12.76	18.94	24.16	– 14.14	– 14.14
80–90	317.10	13.76	124.41	22.38	12.41	19.03	23.94	– 22.35	– 22.35
120–90	268.39	12.49	137.93	16.54	11.24	17.24	22.09	– 32.25	– 32.25
160–90	360.41	14.11	161.38	20.43	13.40	21.14	25.40	– 31.50	– 31.50
200–90	384.01	15.66	203.27	21.31	13.82	19.48	26.34	– 31.94	– 31.94

is considered that there is a significant relationship between the results of the two brittleness indices. In this case, the larger the Kendall's correlation coefficient (ranging from – 1 to 1), the stronger the correlation. In Fig. 9, the Kendall's correlation coefficients for B'_1 and B'_2, B'_4 and B'_5, and B'_3 and B'_6 are all greater than 0.8, with significance values less than 0.01, indicating a high consistency in the evaluation results. The correlation coefficients for other brittleness indices are low, indicating poor consistency. Observing brittleness indices $B_1 - B_6$, we see that B_1 and B_2 are calculated using elastic parameters before the peak of the stress–strain curve; B_4 and B_5 are calculated using stress parameters after the peak of the stress–strain curve; B_3 and B_6 are calculated using energy parameters. This indicates that while the parameters and calculation processes of each brittleness index differ, the brittleness indices derived from the same type of parameters on the stress–strain curve show high consistency under the same test conditions. As shown in Fig. 8a and b, temperatures and BPIs of 120 ℃–60° and 160 ℃–90° are regions with high brittleness under B_1 and B_2 evaluations, while 120 ℃-30° and 160 ℃–45° are regions with low brittleness. In Fig. 8c, temperatures and BPIs of 160 ℃–0°, 30°, and 60° are regions with high brittleness under B_3 evaluation, while 120 ℃–0° and 160 ℃–45° are regions with low brittleness. Figure 8d and e shows that 90° at all temperatures are regions with high brittleness under B_4 and B_5 evaluations, while 80 ℃, 120 ℃–0°, 160 ℃, 200 ℃–45°, and 60° at all temperatures are regions with low brittleness. Figure 8f shows that 160 ℃–60° is a region with high brittleness under B_6 evaluation, while 80 ℃, 120 ℃–0° and 160 ℃, 200 ℃–45° are regions with low brittleness. Although the results of brittleness indices which are based on the same type of parameters of the stress–strain curve show differences, they have consistent trends.

To verify the reliability of brittleness indices evaluation, we analyzed the trends of B'_1-B'_6 for shale samples with all BPIs at 160 °C and shale samples with BPIs of 45° and 90° at different temperatures, showing significant brittleness fluctuations. As shown in Fig. 10a, at 160 °C, the brittleness indices change differently with increasing BPI. The brittleness indices B'_1, B'_2, B'_4 and B'_5 decrease initially and then increase with increasing BPI. The values of these four indices at BPIs of 0° and 30° are almost similar. At a BPI of 45°, B'_4 and B'_5 reach their minimum brittleness values, while B'_1 and B'_2 reach their minimum values at a BPI of 60°. All four indices then sharply increase to their maximum brittleness values at a BPI of 90°. The brittleness indices B'_3 and B'_6 show a different trend. At a BPI of 30°,

Table 4 Calculation results of brittleness indices $B_1 - B_6$ and $(B - B_{\min})/(B_{\max} - B_{\min})$ of all indices

Test condition	B_1	B_2	B_3	B_4	B_5	B_6	$(B - B_{\min})/(B_{\max} - B_{\min})$					
							B'_1	B'_2	B'_3	B'_4	B'_5	B'_6
RT-0	0.85	0.73	2.95	0.21	0.022	10.46	0.54	0.64	0.15	0.20	0.11	0.06
80–0	0.88	0.78	2.11	0.14	0.017	17.32	0.69	0.82	0.46	0.06	0.05	0.19
120–0	0.88	0.77	3.69	0.17	0.014	7.18	0.70	0.76	0	0.12	0	0
160–0	0.83	0.69	1.54	0.38	0.061	42.37	0.48	0.49	0.86	0.54	0.69	0.66
200–0	0.85	0.71	1.93	0.26	0.035	24.17	0.56	0.55	0.56	0.29	0.31	0.32
RT-30	0.82	0.68	1.53	0.37	0.056	34.50	0.41	0.44	0.86	0.51	0.61	0.52
80–30	0.80	0.66	2.29	0.33	0.038	14.77	0.34	0.38	0.38	0.43	0.35	0.14
120–30	0.72	0.56	1.89	0.30	0.032	22.25	0	0	0.58	0.38	0.26	0.28
160–30	0.83	0.68	1.68	0.36	0.054	29.83	0.46	0.45	0.73	0.51	0.58	0.43
200–30	0.83	0.66	1.57	0.31	0.048	36.15	0.45	0.37	0.83	0.40	0.50	0.55
RT-45	0.87	0.75	2.60	0.32	0.034	12.43	0.62	0.69	0.26	0.41	0.29	0.10
80–45	0.86	0.74	1.58	0.36	0.055	32.79	0.60	0.64	0.82	0.51	0.60	0.48
120–45	0.79	0.64	2.12	0.32	0.041	19.06	0.28	0.28	0.45	0.42	0.39	0.22
160–45	0.78	0.63	3.20	0.14	0.015	11.41	0.25	0.26	0.09	0.06	0.02	0.08
200–45	0.76	0.60	2.93	0.25	0.022	11.37	0.18	0.13	0.16	0.28	0.11	0.08
RT-60	0.84	0.71	2.05	0.29	0.038	20.47	0.52	0.54	0.49	0.37	0.35	0.25
80–60	0.85	0.73	1.61	0.21	0.033	36.88	0.56	0.63	0.79	0.20	0.28	0.56
120–60	0.92	0.80	1.85	0.11	0.014	25.97	0.85	0.88	0.61	0	0	0.36
160–60	0.76	0.59	1.40	0.24	0.027	60.16	0.14	0.11	1	0.26	0.18	1
200–60	0.84	0.68	1.53	0.24	0.034	45.07	0.52	0.46	0.86	0.26	0.29	0.72
RT-90	0.89	0.78	2.71	0.36	0.042	14.35	0.75	0.82	0.22	0.51	0.41	0.14
80–90	0.90	0.80	2.07	0.61	0.082	22.73	0.79	0.86	0.48	1	0.99	0.29
120–90	0.90	0.78	1.69	0.49	0.073	32.41	0.78	0.81	0.73	0.76	0.86	0.48
160–90	0.95	0.83	1.81	0.55	0.083	31.75	1	1	0.64	0.89	1	0.46
200–90	0.88	0.74	1.83	0.47	0.071	32.11	0.70	0.66	0.63	0.72	0.82	0.47

these indices decrease slightly, continue to decrease to their minimum values at a BPI of 45°, then sharply rise to their maximum values at a BPI of 60°, and decrease again at a BPI of 90°. As shown in Fig. 10a, the fracture inclinations of shale samples with BPIs of 0°, 30°, 45°, 60°, and 90° at 160 °C are 72°, 63°, 66°, 60°, and 77°, respectively. The fracture planes of shale samples with BPIs of 45° and 60° are parallel to σ_3, while those of samples with other BPIs are parallel to σ_2. Figure 10b shows photos of the fracture surfaces of shale samples with BPIs of 0°, 30°, 45°, and 60° at 160 °C. The fracture surfaces of shale with a BPI of 0° are extremely rough; with a BPI of 30°, slightly rough; and with a BPI of 45°, slightly smooth. Fossils are visible on the fracture surfaces of shale with a BPI of 60°, indicating complete shear along bedding planes and extremely smooth surfaces. Generally, larger fracture inclinations correspond to rougher fracture surfaces and greater rock brittleness (Xia et al. 2017). Therefore, based on fracture inclination and surface roughness, the evaluation results of B_1, B_2, B_4 and B_5 are relatively closest to the observed phenomena. Figure 11a shows the change curves of $B'_1 - B'_6$ for shale samples with a BPI of 45° as temperature increases. B'_1 and B'_2 show a decreasing trend with increasing temperature, while B'_3, B'_4, B'_5 and B'_6 first increase, then decrease, and finally increase again. The fracture inclinations of shale samples with a BPI of 45° at room temperature (RT), 80 °C, 120 °C, 160 °C, and 200 °C are 64°, 68°, 66°, 66°, and 71°, respectively. The evaluation results of B_3, B_4, B_5 and B_6 are consistent with the failure phenomena. Figure 11b shows the change curves of $B'_1 - B'_6$ for shale samples with a BPI of 90° as temperature increases. B'_1 and B'_2 generally increase with temperature, then decrease slightly, increase sharply to their maximum values at 160 °C, and finally decrease. The minimum values occur at 200 °C. B'_3 and B'_6 first increase and then remain stable, with maximum values at 120 °C and minimum values at RT. B'_4 and B'_5 first increase, then decrease, then increase, and finally decrease, with B'_4 peaking at 80 °C and B'_5 nearly peaking at both 80 °C and 160 °C. The minimum values of B'_4 and B'_5 occur at RT. The fracture inclinations of shale samples with a BPI of 90° at RT, 80 °C, 120 °C, 160 °C, and 200 °C are 67°, 80°, 73°, 77°, and 70°, respectively. Tensile-shear composite failure occurs at 80 °C, and tensile failure is generally more brittle than shear failure (Chen et al. 2019). Additionally, shale samples with a BPI of 90° at 80 °C produce audible sounds upon failure, with the sound at 120 °C being significantly less than at 80 °C. At 160 °C and 200 °C,

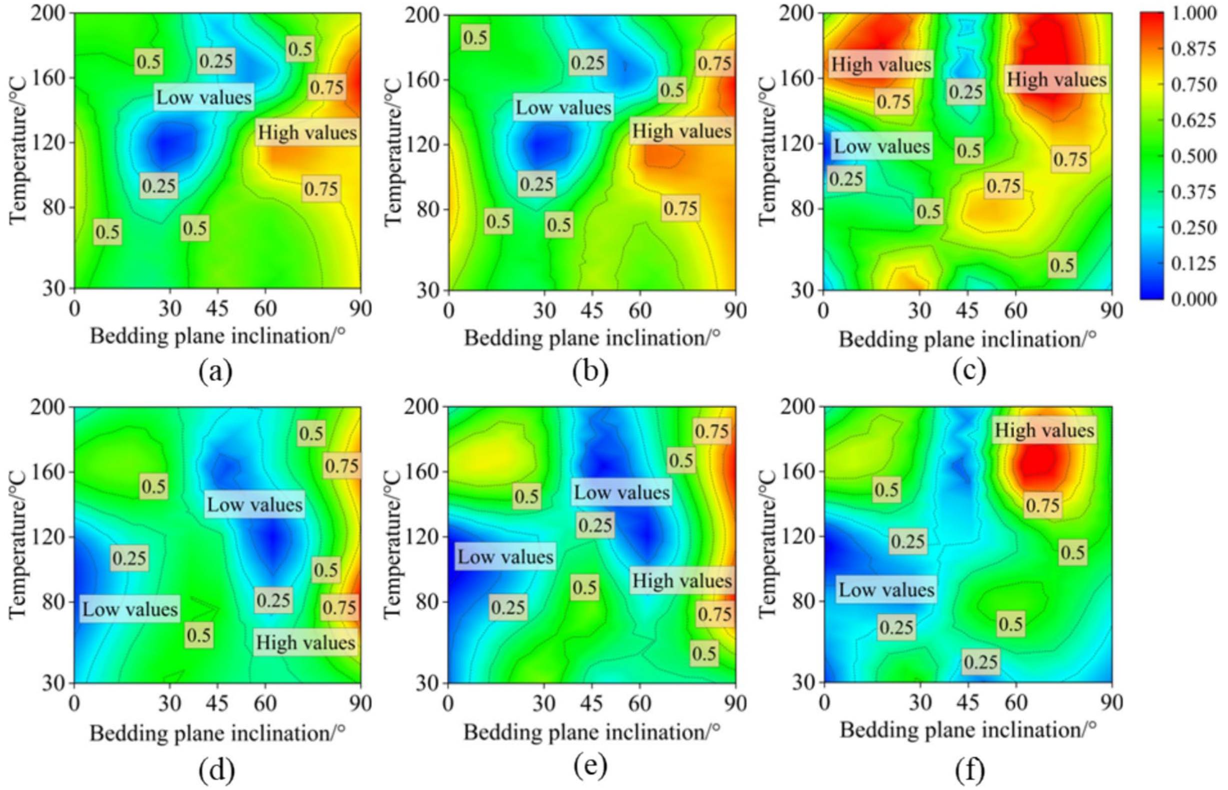

(a) (b) (c) (d) (e) (f)

Fig. 8 Contour maps of normalized brittleness indices of shales under all BPIs and temperatures ranging from RT to 200℃. **a** B'_1, **b** B'_2, **c** B'_3, **d** B'_4, **e** B'_5, **f** B'_6

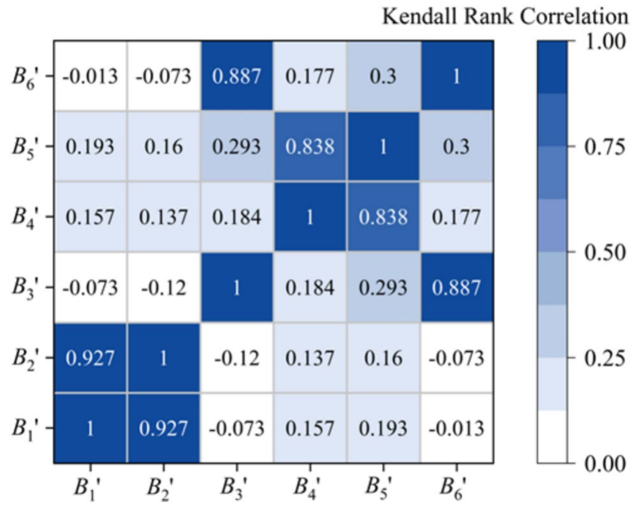

	B_1'	B_2'	B_3'	B_4'	B_5'	B_6'
B_6'	-0.013	-0.073	0.887	0.177	0.3	1
B_5'	0.193	0.16	0.293	0.838	1	0.3
B_4'	0.157	0.137	0.184	1	0.838	0.177
B_3'	-0.073	-0.12	1	0.184	0.293	0.887
B_2'	0.927	1	-0.12	0.137	0.16	-0.073
B_1'	1	0.927	-0.073	0.157	0.193	-0.013

Fig. 9 Heat map of Kendall's τ -b correlation coefficients of brittleness indices $B'_1 - B'_6$

the failure sounds are the most intense. Less brittle rock fails quietly, without debris ejection, and the process is slow (Meng et al. 2015). Thus, based on these phenomena, the evaluation results of B_4 and B_5 align well with the observed phenomena for shale samples with a BPI of 90°. Overall, the brittleness indices B_4 and B_5, which are based on post-peak stress drop and stress drop velocity, provide the best match with the observed failure phenomena under various test conditions. This might be because the observed phenomena are all based on post-peak characteristics of stress–strain curves, such as failure sounds and fracture surface characteristics. Other brittleness indices based on pre-peak parameters and energy ratios do not align with shale fracture characteristics under certain conditions. This discrepancy suggests that the brittleness expression in the post-peak stage under true triaxial loading differs from that in the pre-peak stage. Geng et al. (2016) found that pre-failure elastic parameters alone are insufficient to determine rock brittleness, and it is more reasonable to characterize brittleness based on post-failure behavior.

As shown in Fig. 8d and e, the evaluation results of B_4 and B_5 indicate that the brittleness of shale is significantly influenced by temperature and the distribution of BPI. Under true triaxial loading, σ_2 promotes the rapid aggregation of microcracks, forming a single fracture plane parallel to σ_2, which enhances the rock's brittleness (Vachaparampil and Ghassemi 2017). However, when the BPI is 60°, shale samples exhibit shear failure along the bedding plane at all

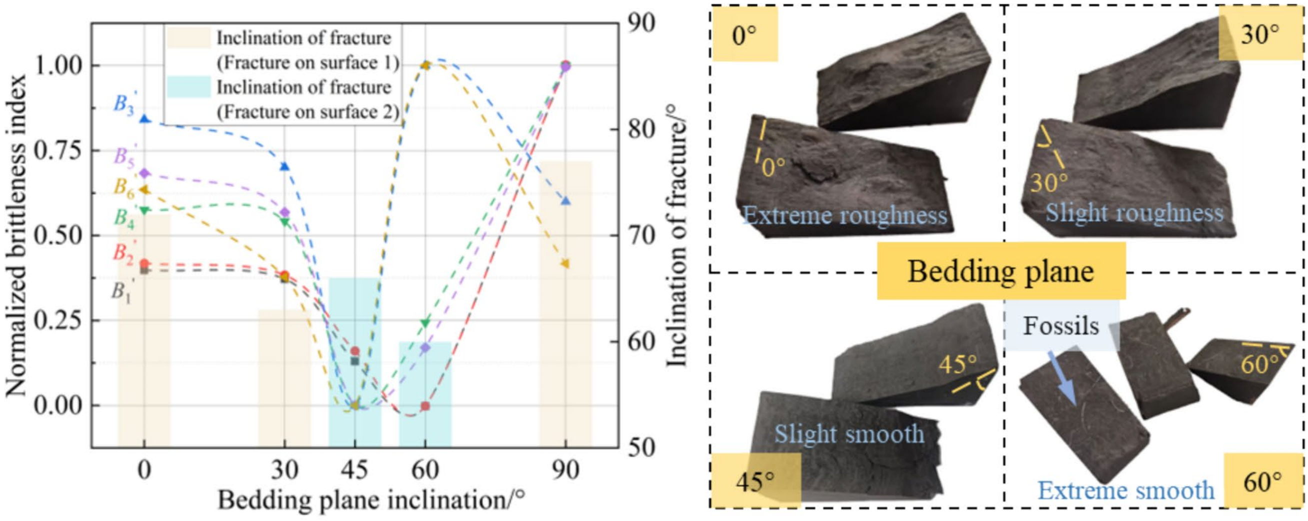

(a) (b)

Fig. 10 Evolution of normalized brittleness indices $B_1' - B_6'$ with BPI at 160 ℃ (**a**), and fracture surface morphology of shales with BPIs of 0°, 30°, 45° and 60° at 160 ℃ (**b**)

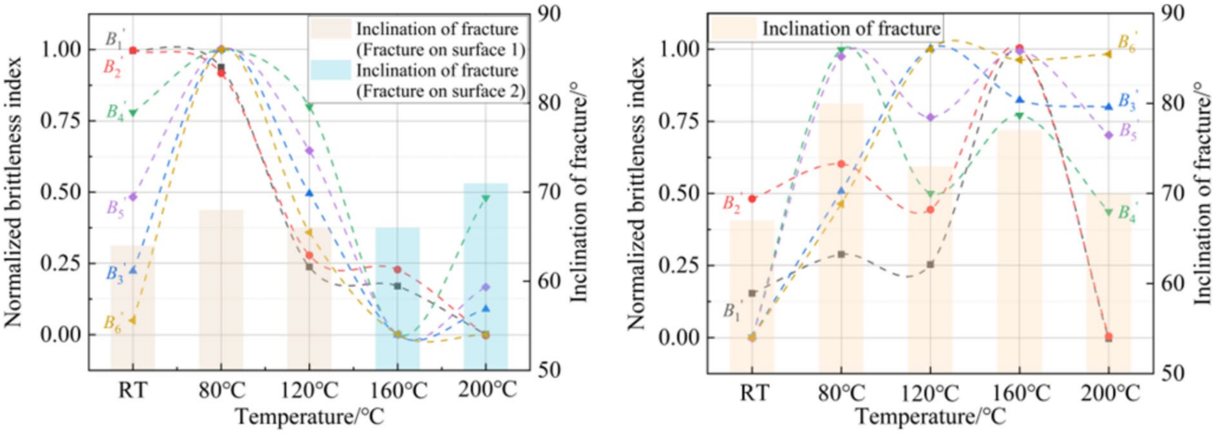

(a) (b)

Fig. 11 Evolution of normalized brittleness indices $B_1' - B_6'$ with temperature in shales with BPIs of 45° (**a**) and 90° (**b**)

temperatures. This behavior is inconsistent with the fracture plane parallel to σ_2 under true triaxial loading, suggesting that the bedding plane at 60° is the least stable. This weakens the brittleness enhancement effect of σ_2 and explains why B_4 and B_5 show a region of low brittleness near a BPI of 60°. The brittleness of shale samples with a BPI of 90° is relatively high at various temperatures. This is because the 90° bedding plane is perpendicular to the σ_2 direction, causing the fracture plane to form parallel to σ_2 and perpendicular to the bedding plane. This configuration releases a significant amount of energy at the moment of failure. Consequently, the failure of shale samples with a BPI of 90° is often accompanied by loud sounds and features such as a sharp post-peak stress drop in the stress–strain curve. Regarding the effect of temperature on shale brittleness, the brittleness of shale samples with a BPI of 0° evaluated by B_4 and B_5 increases at 160 °C and 200 °C. On one hand, the brittle-ductile transformation of rock is primarily controlled by the microcrack propagation and dislocation processes of minerals. Higher temperatures increase the tensile stress between mineral particles (Ma et al. 2023). On the other hand, higher humidity reduces rock brittleness (Xia et al. 2019). As temperature rises, the free water content in shale decreases, and bound water dissipates, resulting in increased brittleness. Shale samples with a BPI of 45° show low brittleness regions at 160 °C and 200 °C because the fracture planes at these temperatures are parallel to the σ_3 direction. This demonstrates that the brittleness of shale samples at different temperatures is the result of the combined effects of temperature and BPI.

5 Discussions

5.1 Influence Mechanism of Temperature on Shale

According to the experimental results in this paper, the influences of temperature on shale samples are reflected in the mechanical properties such as strength, deformation and brittleness. Additionally, the failure mode of some shale samples with specific BPIs, such as those with a BPI of 45°, is strongly affected by temperature. Therefore, this section explores the influence mechanism of temperature on shale in the test and adopts the finite element numerical simulation test method to conduct verification tests under relevant conditions.

5.1.1 Analysis of Test Results

Equation (2) was applied to calculate the normalized coefficient of mechanical properties (NCMP) (Ma et al. 2023), quantifying the continuous changes in the mechanical properties of anisotropic shale samples under varying temperature conditions relative to room temperature (RT).

$$\eta = \frac{(N_i - N_1)}{N_1} \times 100\%, (i = 2,3,4,5) \tag{2}$$

where N_i is the true triaxial compressive strength (TCS) or true triaxial elastic modulus (TEM) of shale samples under the ith temperature, and N_1 is the TCS or TEM of shale sample with different BPIs under RT. As shown in Fig. 12, NCMP values of TCS and TEM of shale samples with BPIs of 0°, 30°, 45°, 60°, and 90° vary with temperature. Blue represents negative values, indicating that mechanical parameters decrease at this temperature compared with RT, while red represents positive values, indicating that mechanical parameters increase. As shown in Fig. 12a, the TCS of most shale samples shows a decreasing trend at 80 ℃ and 120 ℃ compared with RT, and an increasing trend at 160 ℃ and 200 ℃ compared with RT. Except for the shale with a BPI of 45°, TCS presents an upward trend at 120℃ and an upward trend compared with RT at 160℃ and 200℃. The increase amplitudes at 160℃ and 200℃ are larger than those of shale samples with other BPIs, which is probably closely related to the change of failure mode. As shown in Fig. 12b, the TEM of shale samples with BPIs of 0°, 30°, 45°, 60° and 90° at different temperatures has a significantly smaller variation than that of TCS, indicating that TCS of shale is more affected by temperature. The NCMP values of TEM of most shale samples fluctuate in a small range between –10% and 10% at 80 ℃ and 120 ℃ compared with RT. At 160 ℃ and 200 ℃, the TEM values of all shale samples show an obvious upward trend compared with RT, and the rise trend of shale with a BPI of 45° is obvious at 160℃. It is also probably closely related to the shift in the pattern of failure mode.

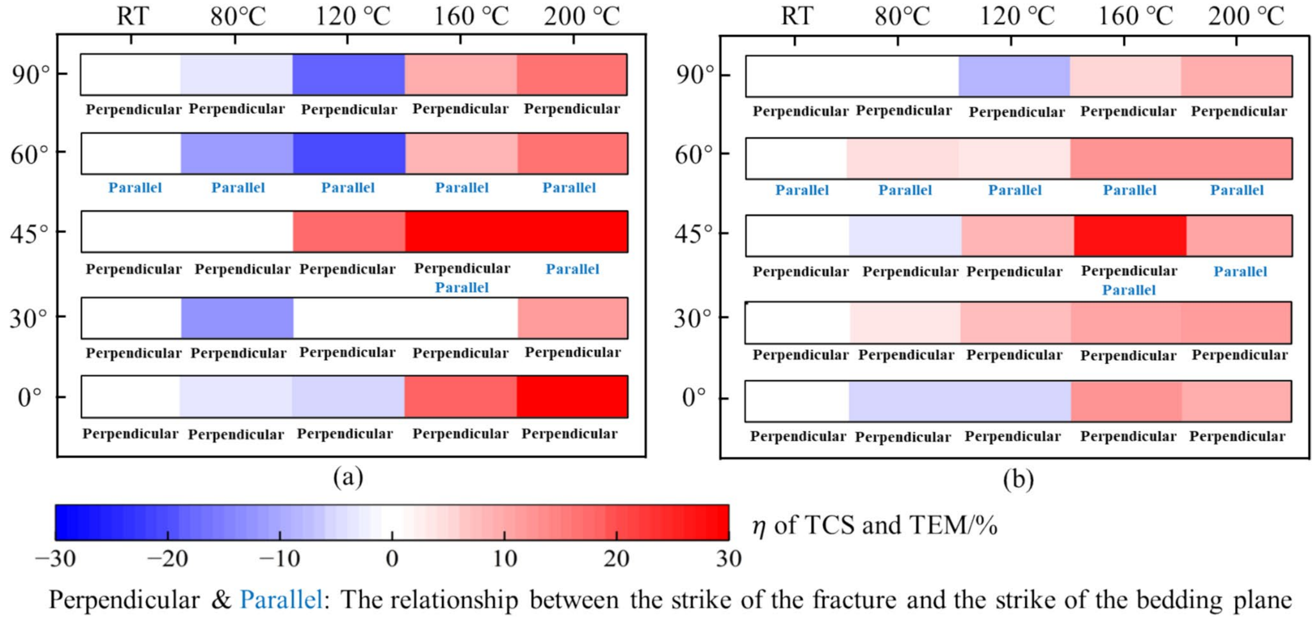

Fig. 12 Normalized coefficient of TCS (**a**) and TEM (**b**) of shales with temperature

As a sedimentary rock rich in clay minerals (Guo et al. 2022b), the water contained in shale is mainly stored in clay minerals (Wang et al. 2020a). This water is mainly divided into free water, interlayer adsorbed water, crystal water and structural water, with interlayer adsorbed water further divided into weakly bound water and strongly bound water (Feng et al. 2018; Fang et al. 2021). Clay minerals include minerals such as montmorillonite, kaolinite and illite, with water absorption capacity decreasing in that order. Hydration of clay minerals can seriously affect the mechanical properties of shale (Zhang et al. 2020; Zhao et al. 2024). Guo et al. (2020) heated the shale samples of the Longmaxi Formation in their natural state and found that their mass decreased by 0.45% at 100 ℃ and 0.92% at 200 ℃ when cooled to RT. This proves that there are free water and interlayer adsorbed water in natural shale of Longmaxi Formation. Due to the different composition of clay minerals, the thermogravimetric analysis results also differ. In general, the complete dissipation temperature range of free water in clay minerals is 70℃–84℃, the complete dissipation temperature range of weakly bound water is 118℃–140℃, and the strongly bound water can completely dissipate at 230 ℃ (Wang and Xiong 2002; Li et al. 2012b; Zhu et al. 2020; Shi 2023). Therefore, the possible reason for the slight decline in TCS at 80 ℃ is that the temperature rise leads to the extension and expansion of micro-cracks, making shale samples more vulnerable to destruction (Guo et al. 2020; Ma et al. 2023). The presence of microcracks also leads to a decline in cohesion between rock particles (Meng et al. 2019; Zhao et al. 2023a). Secondly, free water evaporation in the shale matrix leads to an increase in porosity and a decrease in shale integrity. In addition, even if the internal free water of shale samples evaporates at 80 ℃, the bound water has not completely dissipated at this temperature, and the low permeability of shale during loading will lead to excessive pore pressure in some areas, resulting in reduced effective stress and easier fracture of shale (Zhang et al. 2020). At 120 ℃, TCS is generally still lower than RT, which may be due to the further extension and expansion of micro-cracks caused by rising temperature, resulting in a decline in strength, and weakly bound water in clay minerals in shale matrix is not completely dissipated, resulting in lubrication. At 160 ℃ and 200 ℃, TCS increase compared to RT, because the weakly bound water of clay minerals in the shale matrix completely dissipates at this temperature, while the strongly bound water also begins to dissipate, resulting in a decrease in the adverse factors to strength. Among them, the shale with a BPI of 45° presents a TCS greater than RT at 120 ℃, which may be because the fracture direction of the shale with a BPI of 45° changes with the increase of temperature, resulting in an increase in the macroscopic strength. As for the TEM, there is almost no significant change under the lower temperature loading at 80 ℃ and 120 ℃. However, at 160 ℃ and 200 ℃, TEM of all shale samples is generally higher than RT, which may be due to the dissipation of weakly and strongly bound water, which weakens the lubrication effect of the internal particles of shale samples, making deformation difficult, and finally, the macro TEM becomes larger. The TEM of shale with a BPI of 45° is significantly greater than RT at 160 ℃, indicating that the change of fracture direction can significantly affect the mechanical properties of shale. In addition, after macroscopic shear failure of shale samples, stick–slip phenomena generally occurred in the post-peak residual stage at 120 ℃ and higher temperatures with further loading of vertical displacement, as shown in Fig. 4. Wei et al. (2024) studied the shear mechanical properties of illite with different interlayer water content through molecular dynamics simulation and found that illite containing weakly bound water and free water between layers generally had a weak stick–slip effect, because weakly bound water and free water mainly played a lubricating role in the shear process, while illite containing strongly bound water between layers had the strongest stick–slip effect. Therefore, the free water evaporates completely and the weakly bound water partially dissipates at 120 ℃, and the stick–slip phenomenon begins to appear in the residual section after the peak. The weakly bound water dissipates completely at 160 ℃, and the stick–slip effect becomes more obvious.

According to the failure modes shown in Fig. 7, the failure mode of shale samples is influenced by temperature and the distribution of BPI. The failure mechanisms of anisotropic shale under the influence of temperature were explored. Figure 13a presents the true triaxial loading diagram of a shale sample with a BPI of β, assuming only one bedding plane inside the shale. There are two possible failure modes based on the σ_2 direction, which is perpendicular to the strike of the bedding plane. The first mode involves shear or tensile failure of the fracture plane, with the strike parallel to the σ_2 direction. This is caused by the deformation inhibition of σ_2 in this direction, leading to fracture planes forming in the shale matrix and intersecting with the bedding plane (Fig. 13a). The second mode involves shear failure when the fracture plane forms entirely along or near the bedding plane under its influence, with the strike of the fracture plane parallel to σ_3 (Fig. 13a). Since the fracture planes formed by these two failure modes strike in opposite directions, the final failure form of shale is determined by the competition between these modes.

Next, the shear failure along the bedding plane is analyzed. Since σ_3 is loaded parallel to the bedding plane, it is assumed that σ_3 does not affect the stress distribution on the bedding plane. The cross-section of the shale is obtained by cutting it perpendicularly along the σ_3 direction, simplifying it to a two-dimensional plane problem as shown in Fig. 13a. Jager (1979) proposed the formulas

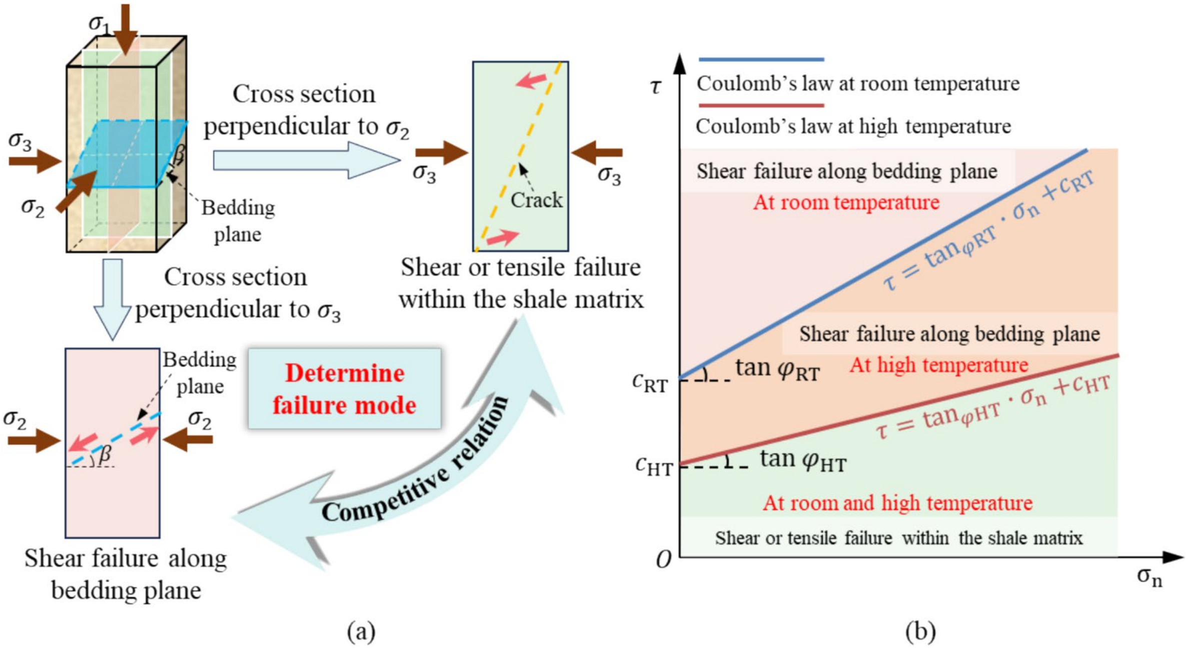

Fig. 13 Analysis of possible failure modes of shale with an idealized single bedding plane (**a**) and variation of Coulomb's law of the bedding surface affected by temperature (**b**)

for normal stress and shear stress on a single inclined plane loaded by two-dimensional plane principal stress as follows:

$$\sigma_{\text{n}} = \frac{1}{2}\left(\sigma_1 + \sigma_2\right) + \frac{1}{2}\left(\sigma_1 - \sigma_2\right)\cos 2\beta \tag{3}$$

$$\tau = \frac{1}{2}\left(\sigma_1 - \sigma_2\right)\sin 2\beta \tag{4}$$

where, σ_{n} is the normal stress on the bedding plane, τ is the shear stress on the bedding plane, and β is the angle between the bedding plane and the horizontal plane. When shear failure occurs along the bedding plane, the strength of the bedding plane conforms to the Coulomb's law, as shown in Eq. (5):

$$\tau = \sigma_{\text{n}}\tan\varphi + c \tag{5}$$

where, φ is the internal friction angle of the bedding plane, and c is the cohesion of the bedding plane. Guo et al. (2022b) substituted Eqs. (3) and (4) into Eq. (5) to obtain the Coulomb's law expressed by principal stress and β (Eq. (6)), and then took the derivative of Eq. (6) with respect to β to obtain the BPI of $\alpha = \frac{\pi}{4} + \frac{\varphi}{2}$ at the smallest σ_1. According to the internal friction angle of the bedding plane of shale from the Longmaxi Formation at RT being about 30°, the most unfavorable BPI under RT is about 60° (Guo et al. 2022b).

$$\sigma_1 = \sigma_2 + \frac{2\left(c+\sigma_2\tan\varphi\right)}{(1-\tan\varphi\cos\beta)\sin 2\beta} \tag{6}$$

In the direct shear test, the shear strength of the bedding plane of shale is significantly lower than that of the shale matrix (Lu et al. 2021). When the Bedding Plane Inclination (BPI) of shale is 60°, the required σ_1 for shear failure along the bedding plane is the smallest. Therefore, under the loading of σ_1, the sliding force on the bedding plane exceeds the shear strength, causing shear failure before the shear or tensile microcracks parallel to σ_2 in shale aggregate through. This explains the shear failure of shale with a BPI of 60° along the bedding plane at room temperature (RT). Experimental studies on sedimentary rock (sandstone) with well-developed bedding planes after heating showed that the internal friction angle of sandstone samples with 0°, 45°, and 60° angles between the bedding plane and the horizontal plane decreased with increasing temperature in the range of RT-200 °C (Yang et al. 2017; Qin et al. 2023). For most rocks, temperature increase leads to the formation of thermal cracks, increasing the distance between molecules and effectively reducing rock cohesion (Meng et al. 2019; Zhao et al. 2023a). As shown in Fig. 13b, the blue line represents Coulomb's law for the bedding plane of shale with a BPI of 60° at RT: $\tau = \sigma_{\text{n}}\tan\varphi_{\text{RT}} + c_{\text{RT}}$. The red line represents Coulomb's law for the bedding plane of shale with a BPI of 60° under real-time heating: $\tau = \sigma_{\text{n}}\tan\varphi_{\text{HT}} + c_{\text{HT}}$. The region above the blue line indicates shear failure along the bedding plane when shear strength is reached at RT, with $\tau_{\text{RT}-60^\circ} \geq \sigma_{\text{n}-60^\circ}\tan\varphi_{\text{RT}} + c_{\text{RT}}$. If c_{RT} decreases to c_{HT} with increasing temperature, and $\tan\varphi_{\text{RT}}$ decreases to

$\tan\varphi_{HT}$, assuming the strength σ_1 remains constant, then $\tau_{RT-60^\circ} > \sigma_{n-60^\circ}\tan\varphi_{HT} + c_{HT}$ causes shear failure along the bedding plane. Thus, the area between the blue and red lines represents shear failure along the bedding plane of shale with a BPI of 60° caused by a decline in shear strength at high temperature.

According to the most unfavorable inclination $\alpha = \frac{\pi}{4} + \frac{\varphi}{2}$, if the internal friction angle decreases with increasing temperature in the range of RT-200 °C, the most unfavorable inclination angle α will develop to be less than 60°. Under the loading of σ_1, if the shear or tensile microcracks parallel to σ_2 aggregate first, the failure forms of shale with BPIs of 0° and 30° at RT-200 °C and shale with a BPI of 45° at RT-120 °C will appear, corresponding to the area below the red line in Fig. 13b. As the cohesion of the bedding surface further weakens with temperature. If shear failure along the bedding plane in the σ_3 direction occurs almost simultaneously with microcracks parallel to the σ_2 direction, then shale with a BPI of 45° at 160 °C will have fractures in all directions (Fig. 13b). If shear failure occurs first along the bedding plane in the σ_3 direction, the failure forms of shale with a BPI of 45° at 200 °C (Fig. 13b) and shale with a BPI of 60° at 80 °C–200 °C correspond to the middle region of the blue and red lines in Fig. 13b. The region above the blue line in Fig. 13b corresponds to the shear failure of shale with a BPI of 60° along the bedding plane at RT. Therefore, the failure forms of anisotropic shale at different temperatures are closely related to the variation of shear strength of the bedding plane with temperature. This analysis is based on the variation in the cohesion observed in experiments after heating sedimentary rock. Currently, there are few experiments on the variation in the cohesion of shale at real-time temperatures, so further research and verification are needed.

5.1.2 Analysis of Numerical Simulation Results

To verify the effect of temperature and BPI on the mechanical properties of shale under true triaxial loading, true triaxial tests of shale under relevant in situ stress and temperature were carried out using numerical simulation. RFPA (Realistic Failure Process Analysis) is a finite element numerical analysis software developed by Tang and Kaiser (1998) and Li et al. (2012a), which incorporates statistical mesoscopic damage theory. It considers the non-uniformity of rock materials by setting the coefficient of heterogeneity m in the Weibull distribution, as shown in Eq. (7):

$$\varphi(u) = \frac{m}{u_0}\left(\frac{u}{u_0}\right)^{m-1} exp\left[-\left(\frac{u}{u_0}\right)\right]^{m-1} \tag{7}$$

Here, u represents the mechanical parameter of an element; u_0 represents the average value of the input mechanical parameter; m is the coefficient of heterogeneity, and the larger the m value, the more uniform the distribution of the mechanical parameter of the elements.

RFPA^{3D}-Thermal is a numerical analysis version of RFPA that considers temperature effects. By introducing thermophysical parameters such as thermal conductivity coefficient, volumetric heat capacity and thermal expansion coefficient, the three-dimensional numerical simulation analysis of rock failure under the coupled conditions of temperature and stress fields can be carried out (Chen et al. 2024). In RFPA^{3D}-Thermal, the unsteady heat conduction equation for a model without an internal heat source is shown in Eq. (8):

$$\frac{\partial}{\partial x}\left(\lambda\frac{\partial T}{\partial x}\right) + \frac{\partial}{\partial y}\left(\lambda\frac{\partial T}{\partial y}\right) + \frac{\partial}{\partial z}\left(\lambda\frac{\partial T}{\partial z}\right) = \rho C\frac{\partial T}{\partial t} \tag{8}$$

where T is the temperature of the material,℃; ρ is the material density, kg/m^3; C is the specific heat capacity, J/(kg · K); λ is the thermal conductivity coefficient, W/(m · K); t is the time of unsteady heat transfer, s; x, y and z are the coordinates of elements in the rectangular coordinate system.

The element in RFPA^{3D}-Thermal adopts the thermoelastic theory constitutive equation, as shown in Eq. (9):

$$\sigma_{ij} = \lambda'\varepsilon_{kk}\delta_{ij} + 2G\varepsilon_{ij} - \gamma\Delta T\delta_{ij} \tag{9}$$

where σ_{ij} is stress; ε_{ij} is strain; λ' is the Lame coefficient $\left(\lambda' = \frac{E\mu}{(1+\mu)(1-2\mu)}\right)$, with μ being the Poisson's ratio; G is the shear modulus $\left(G = \frac{E}{2(1+\mu)}\right)$; γ is the thermal stress coefficient $\left(\gamma = \frac{E\alpha}{1-2\mu} = (3\lambda + 2G)\alpha\right)$, with α being the thermal expansion coefficient, δ_{ij} is the Kronecker function

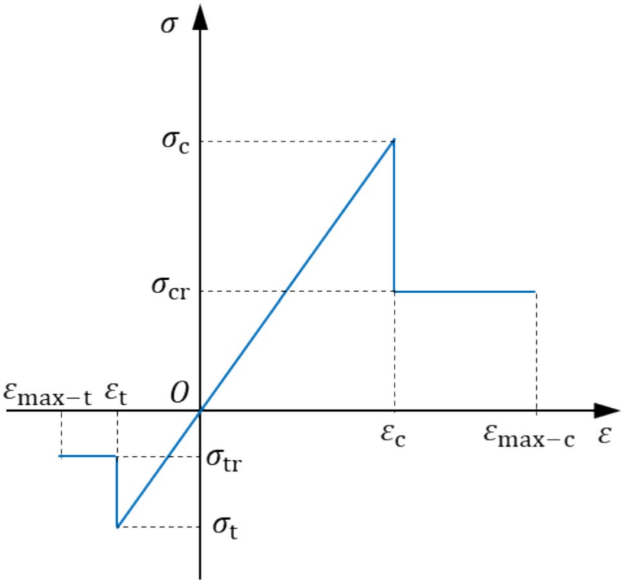

Fig. 14 Elastic-brittle constitutive relationship of elements in RFPA

($\delta_{ij} = \begin{cases} 0 \, i \neq j \\ 1 \, i = j \end{cases}$), and ΔT is the temperature difference. Figure 14 shows the elastic-brittle constitutive relation curve of the elements under loading. The failure of the elements is divided into compressive shear failure and tensile failure. Tensile failure is judged by the maximum tensile stress criterion, while shear failure is judged by the Mohr–Coulomb criterion. After the elements reach compressive shear or tensile failure, their strength reduces to the residual compressive strength σ_{cr} or the residual tensile strength σ_{tr}. Over the years, RFPA has been successfully applied to rock engineering deformation and failure instability analysis (Xia et al. 2017; Zhao et al. 2022a, 2022b, 2023b; Chen et al. 2024).

Figure 15a shows the shale numerical samples with BPIs of 0°, 30°, 45°, 60°, and 90°. The size of the numerical samples is 50 mm × 50 mm × 100 mm, the same as that of the physical samples, and the numerical samples are divided into 100 × 100 × 200 = 2,000,000 hexahedral elements. The bedding plane width is two elements, with a width of 1 mm. According to the bedding plane spacing of Longmaxi Formation shale, which is about 4–7 mm (Wang et al. 2023), the bedding plane spacing of numerical samples was determined to be 5 mm. Three fixed displacement boundaries in the *x*, *y* and *z* directions were adopted for the numerical samples. The confining pressure loading rate is 5 MPa/step, and the target stress and direction are the same as in the previous physical tests. The first boundary condition of heat transfer was adopted for the numerical samples, and temperature loading was carried out on the four sides before loading. The temperature loading rate is 5 ℃/step, and the initial temperature of the models is 20 ℃. Before loading, the confining pressure and temperature were loaded simultaneously. When the target stress and temperature were reached, the confining pressure and temperature were kept constant, and vertical displacement loading with 0.02 mm/step in the y direction was carried out until failure. According to the tests results of BSE (Back Scattered Electron) images and energy spectrometric scanning images conducted by Yin (2020) on the shale of Longmaxi Formation, the quartz content in the shale matrix of Longmaxi Formation occupies the largest proportion. Therefore, quartz mineral was taken as the representative of the thermophysical parameters of the shale matrix in this paper. The bedding plane

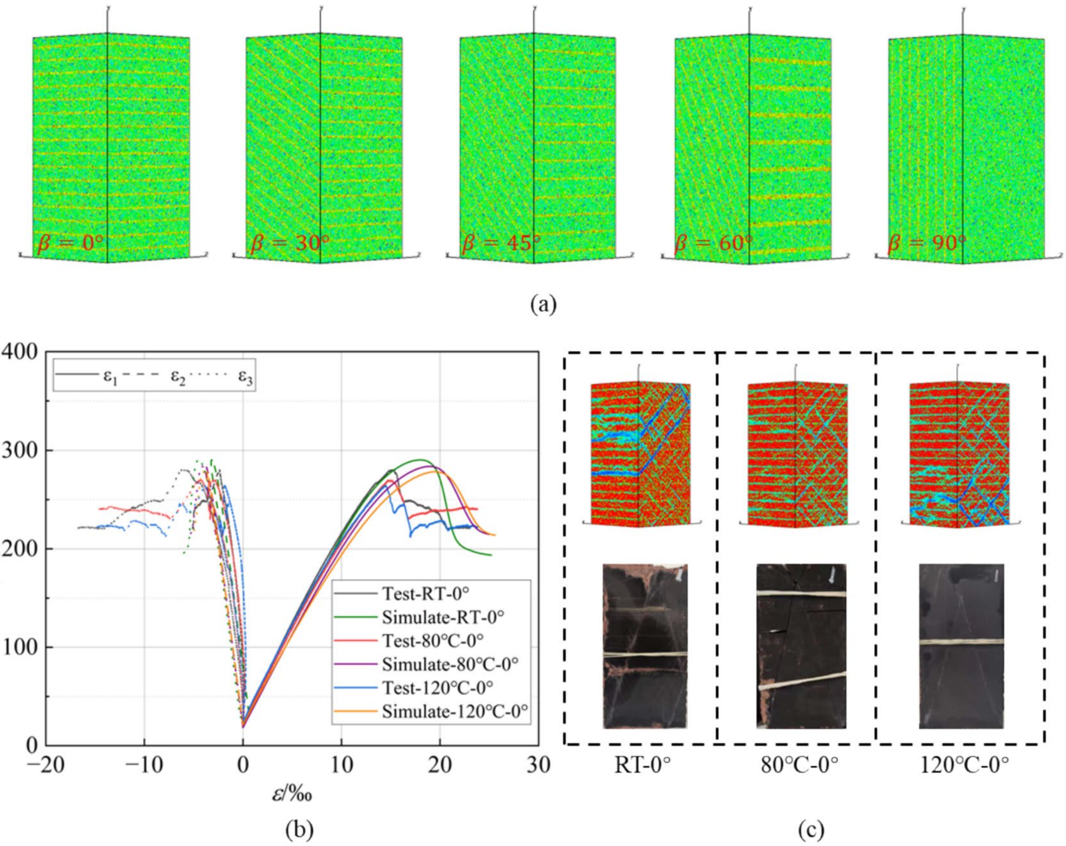

(a)

(b)

(c)

Fig. 15 Shale numerical samples with BPIs of 0°, 30°, 45°, 60° and 90° (**a**), test and simulation of stress–strain curves (**b**) and failure morphologies (**c**) of shales with a BPI of 0° at 20 ℃, 80 ℃ and 120 ℃ under true triaxial loading of Longmaxi Formation shale mainly consists of calcite and a small amount of pyrite, so calcite mineral was taken as the representative of the thermophysical parameters of the bedding plane. The thermal conductivity coefficient of quartz is 7.69 W/(m · K); the linear expansion coefficient is 24.3×10^{-6} /K; the specific heat capacity is 632.4 J/(kg · K); the density is 2.65 g/cm^3; and the converted volumetric heat capacity is 1.68×10^{6} J/(m^3 · K). The thermal conductivity coefficient of calcite is 3.57 W/(m · K); the linear expansion coefficient is -3.2×10^{-6} /K; the specific heat capacity is 834.2 J/(kg · K); the density is 2.71 g/cm^3; and the converted volumetric heat capacity is 2.26×10^{6} J/(m^3 · K) (Sydney 1966; Yu 2015; Selvadurai and Rezaei 2020; Wang 2021). The mechanical parameters of the models were obtained by trial and error method (Zhao et al. 2023b), and stress–strain curves and failure modes of shale numerical samples with a BPI of 0° at different temperatures were compared with the physical test results (Fig. 15b and c). Finally, the calibrated mechanical parameters adopted in the subsequent simulation were obtained, as shown in Table 5.

Figure 16a–e shows the true triaxial stress–strain curves of shale with BPIs of 0°, 30°, 45°, 60° and 90° at real-time temperatures of 20 ℃, 80 ℃, 120 ℃, 160 ℃ and 200 ℃, respectively. The numerical samples under true triaxial loading exhibit the same behavior as the physical samples, showing three stages: elastic deformation, unstable fracture development, and residual deformation. Moreover, under the influence of σ_2, the peak strain of the numerical samples in the direction of σ_2 is significantly smaller than that in the

Table 5 Mechanical parameters used in the numerical simulation

Structures	Elastic Modulus/MPa	Compressive Strength/MPa	Poisson's Ratio	Fraction Angle/°	C-T ratio	Residual Strength/%
Shale matrix	23,800	330	0.25	30	9	0.6
Heterogeneity index	4	4	200	/	/	/
The bedding plane	14,280	198	0.27	26	10	0.6
Heterogeneity index	3	3	200	/	/	/

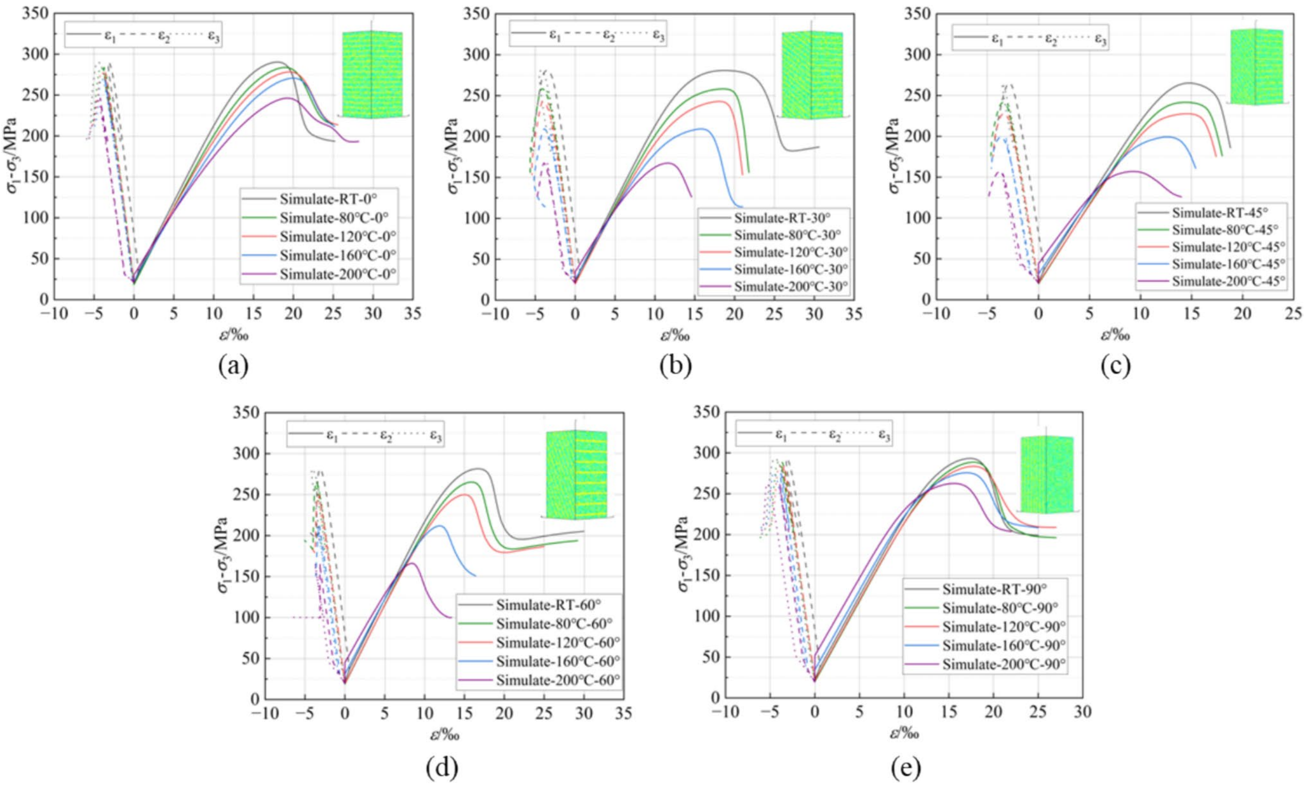

Fig. 16 Stress–strain curves of shales with BPIs of 0° (**a**), 30° (**b**), 45° (**c**), 60° (**d**), 90° (**e**) at 20 ℃, 80 ℃, 120 ℃, 160 ℃ and 200 ℃ in numerical stimulation

Table 6 Strength and deformation parameters obtained from the numerical simulation

Test condition	σ_p/MPa	E/GPa	$\varepsilon_1/10^{-3}$
RT-0	290.35	19.10	18.00
80–0	283.79	18.47	19.00
120–0	278.29	17.42	19.40
160–0	270.75	16.25	20.00
200–0	246.28	14.86	19.20
RT-30	280.83	19.16	18.80
80–30	258.33	18.72	18.60
120–30	242.96	17.96	18.00
160–30	209.31	16.89	15.80
200–30	167.56	15.52	11.60
RT-45	265.29	19.64	14.80
80–45	241.68	19.41	14.40
120–45	227.74	18.97	14.60
160–45	199.30	18.21	12.60
200–45	157.00	17.12	9.20
RT-60	281.57	19.41	16.60
80–60	265.27	19.23	15.80
120–60	249.96	18.92	15.00
160–60	211.87	18.26	11.80
200–60	166.31	17.21	8.40
RT-90	293.32	19.72	17.40
80–90	288.72	19.67	17.80
120–90	283.67	19.62	17.80
160–90	275.79	19.46	17.00
200–90	262.66	18.99	15.60

direction of σ_3, which aligns with the deformation characteristics of true triaxial loading. The peak strength and elastic modulus of the numerical samples are shown in Table 6. The peak strength of the shale samples decreases significantly with increasing temperature at 20 ℃–120 ℃, which is roughly consistent as the physical samples. The peak strength of the numerical samples continues to decrease at 160 ℃ and 200 ℃, but the peak strength increases significantly in the physical tests. Figure 16a–e shows that the peak strength of the numerical samples with BPIs of 30°, 45° and 60° decreases more significantly with temperature than that of 0° and 90°. This is because the linear expansion coefficients of the bedding plane and the matrix are different, and the amount of thermal deformation varies, resulting in greater thermal stress near the interface between the bedding plane and the matrix. However, the numerical samples with BPIs of 30°, 45°, and 60° have a greater bedding plane angle, so the changes caused by thermal damage to the bedding plane have a more intense impact on the overall strength of the numerical samples. In contrast, numerical samples with BPIs of 0° and 90° are perpendicular or parallel to the loading direction, so the thermal damage to the bedding plane has less impact on the overall strength of the numerical samples compared with those with large BPI. This simulation only considers the thermal stress of the materials, so as the temperature increases to 200 ℃, the area and degree of thermal damage also increase, resulting in a decrease in the peak strength of the numerical samples. According to the physical experiment results, the complete dissipation of weakly bound water under the influence of a certain temperature range is largely responsible for the increase in the peak strength of shale samples. Unfortunately, it is currently difficult to implement numerical analysis software for rock mechanics that considers the change of free water and interlayer adsorbed water with temperature, which can be considered as future research. The numerical samples in this paper only consider the effect of thermal stress on shale, which also reflects that the water content of clay minerals inside shale may have a significant influence on the change in mechanical properties of shale at real-time high temperatures.

Figure 17 shows the failure modes of the numerical samples with BPIs of 0°, 30°, 45°, 60°, and 90° at real-time temperatures of 20 ℃, 80 ℃, 120 ℃, 160 ℃, and 200 ℃. The failure modes can be divided into cutting through the shale matrix and shear along the bedding plane. The failure modes of the numerical samples with BPIs of 0° and 90° at 20 ℃–200 ℃ are cutting through the shale matrix, with several inclined shear fractures appearing parallel to σ_2, which is related to the deformation inhibition of σ_2 and aligns with the deformation and failure results of physical tests under true triaxial loading. The numerical samples with BPIs of 30°, 45°, and 60° at 20 ℃–200 ℃ mainly fail by shearing along the bedding plane. The numerical samples with a BPI of 30° slip along the bedding plane at 20 ℃ and 80 ℃, accompanied by some shear fractures parallel to σ_2. However, with increasing temperature, the shear fractures parallel to σ_2 gradually decrease and disappear. The reason is that with increasing temperature, the thermal damage caused by the different linear expansion coefficients between the bedding plane and the matrix intensifies, making the shale more prone to sliding along the bedding plane. Tish is also consistent with the physical test results and further indicates that the influence of temperature on the thermal damage of the bedding plane is more severe. Figure 18 shows the results of stress, damage and element microfracture of the numerical samples with a BPI of 60° during heating to 200 ℃. The stress distribution of the sample at 20 ℃ is uniform, and no element failure occurs. At 80 ℃, obvious stress concentration appears at the position of the bedding plane, and compressive shear failure occurs in some internal elements of the sample. At 120 ℃, 160 ℃, and 200 ℃, the stress concentration at the bedding plane becomes increasingly pronounced because the strength of the bedding plane is significantly lower than that of the matrix, resulting in an

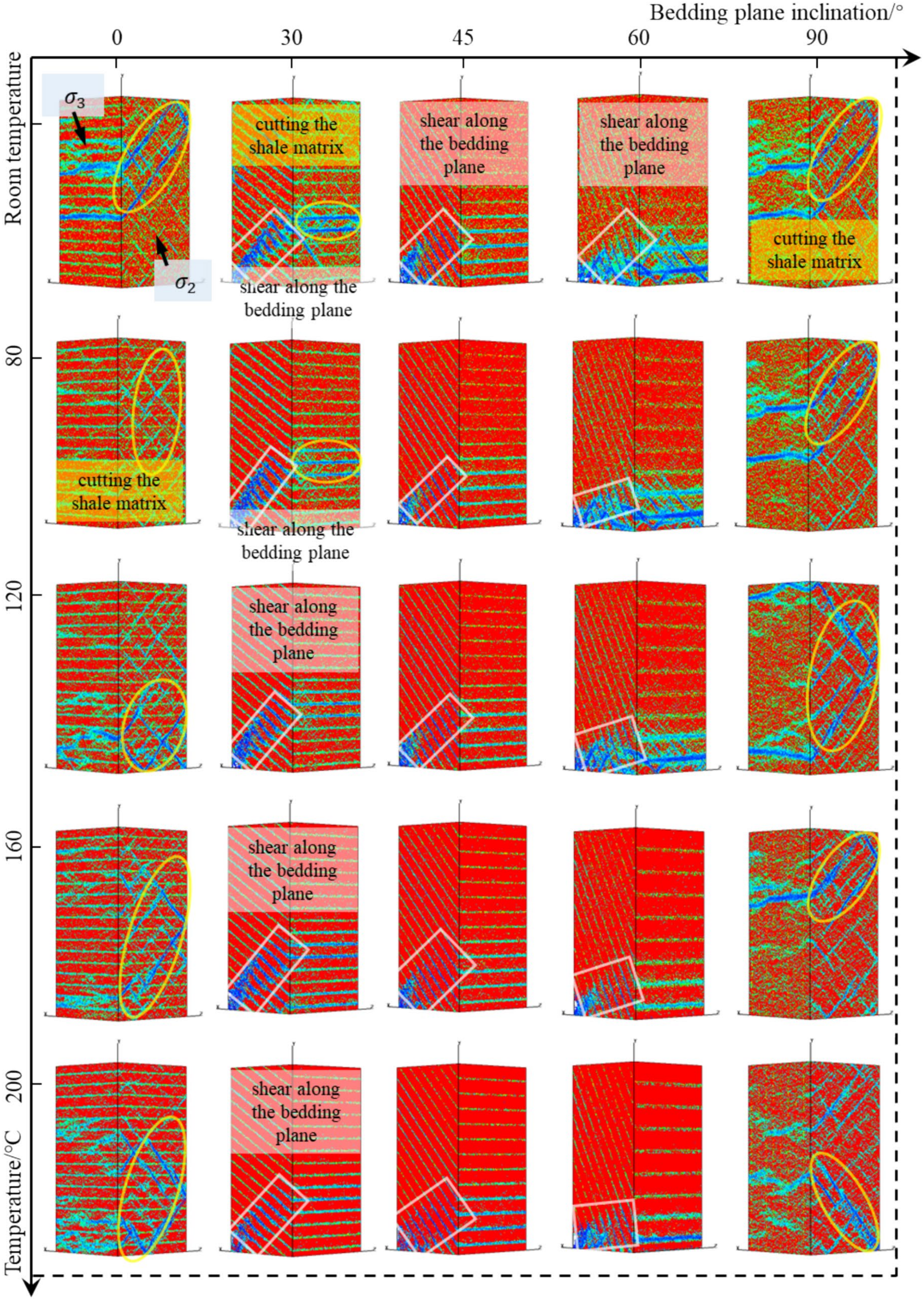

Fig. 17 Failure morphologies of shales under all BPIs and temperatures ranging from 20 ℃ to 200 ℃ in the numerical stimulation

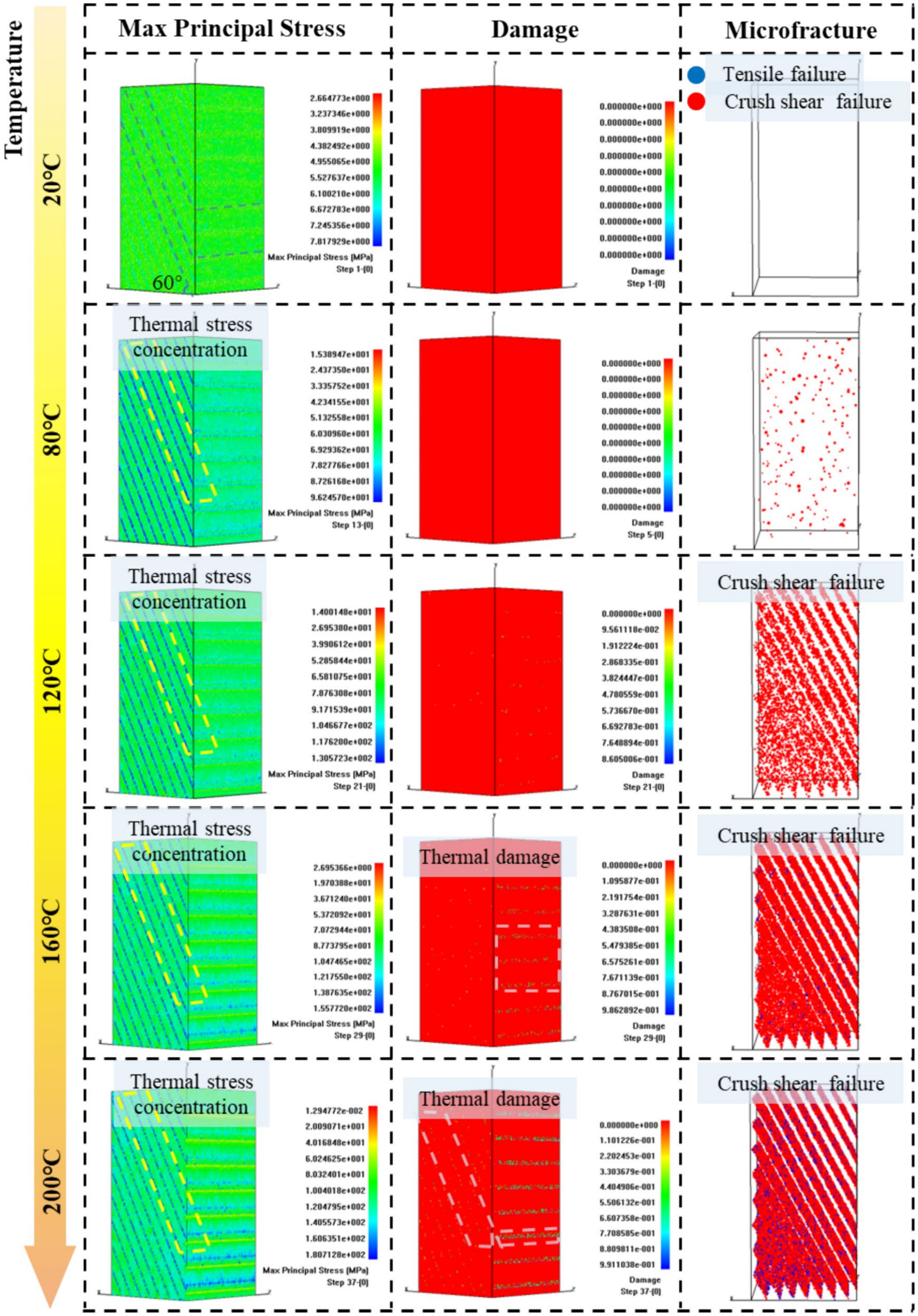

Fig. 18 Maximum principal stress contours, damage contours, and microfracture contours of shales with a BPI of 60° at RT, 80 ℃, 120 ℃, 160 ℃ and 200 ℃ in numerical stimulation

increasing number of damaged elements along the bedding plane, showing the compressive shear failure of the bedding plane elements. This also indicates that, without considering the influence of internal water, the failure mode in physical tests tends to slip along the bedding plane more easily with increasing temperature because of the thermal stress concentration between the bedding plane and the matrix.

5.2 Variation of Temperature on Shale Anisotropy

To quantify the continuous changes in the mechanical properties of shale samples with different BPIs, the normalized coefficients of mechanical properties (NCMP) compared to a BPI of 0° were calculated. As shown in Fig. 19a, TCS of shale samples with BPIs of 30°, 45°, and 60° at RT, 80 ℃, 160 ℃, and 200 ℃ is smaller than that of shale samples with a BPI of 0°, while the TCS of shale samples with a BPI of 90° is larger than that of shale samples with a BPI of 0°. At 120 ℃, the variation of TCS of shale samples with BPI is inconsistent with other angles. As shown in Fig. 19b, the variation of TEM of shale samples with BPI is roughly consistent with that of TCS. Except at 120 ℃, the TEM of shale samples with BPIs of 30° and 45° is smaller than that of shale samples with a BPI of 0°, while the TEM of shale samples with BPIs of 60° and 90° is larger than that of shale samples with a BPI of 0°. It can be seen that under true triaxial loading with a high horizontal stress difference of 20 MPa, except at 120 ℃, the most adverse BPI for shale's mechanical properties is 30°–45°. The special behavior at 120 ℃ may be due to the temperature range for the complete dissipation of weakly bound water being 118 ℃–140 ℃ (Wang and Xiong 2002; Li et al. 2012b; Zhu et al. 2020; Shi 2023). Therefore, affected by individual differences in shale samples, the degree of dissipation of weakly bound water varies at 120 ℃, resulting in different degrees of influence on mechanical properties. Only free water evaporates at 80 ℃, while weakly bound water does not dissipate in large quantities. At 160 ℃ and 200 ℃, weakly bound water dissipates completely. This ultimately explains the change in anisotropic shale under true triaxial loading.

To investigate whether temperature affects the anisotropy of shale under true triaxial loading, Eqs. (10) and (11) were used to calculate the degree of anisotropy of true triaxial compressive strength ($R_{C(\text{TCS})}$) and true triaxial elastic modulus ($R_{C(\text{TEM})}$) of shale samples, respectively (Saroglou and Tsiambaos 2008):

$$R_{C(\text{TCS})} = \frac{\text{TCS}_{\text{max}}}{\text{TCS}_{\text{min}}} \tag{10}$$

$$R_{C(\text{TEM})} = \frac{\text{TEM}_{\text{max}}}{\text{TEM}_{\text{min}}} \tag{11}$$

where TCS_{max}, TCS_{min}, TEM_{max}, and TEM_{min} are the maximum and minimum values of TCS and TEM of anisotropic shale samples at the same temperature, respectively. The $R_{C(\text{TCS})}$, $R_{C(\text{TEM})}$ and the BPI corresponding to the maximum and minimum values are plotted as a variation chart with temperature, as shown in Fig. 20. The maximum values of TCS and TEM occur at a BPI of 90°, while the minimum values of TCS and TEM occur at BPIs of 30° and 45°. Both $R_{C(\text{TCS})}$ and $R_{C(\text{TEM})}$ show a decreasing trend with increasing

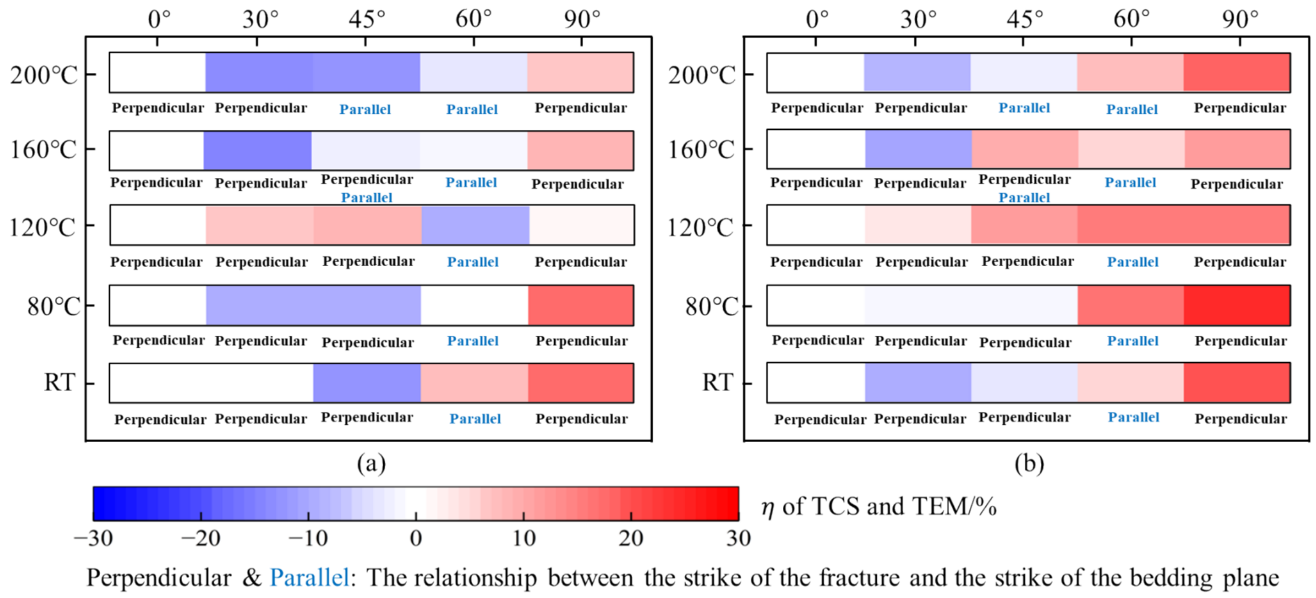

Fig. 19 Normalized coefficients of TCS (**a**) and TEM (**b**) of shales with BPI

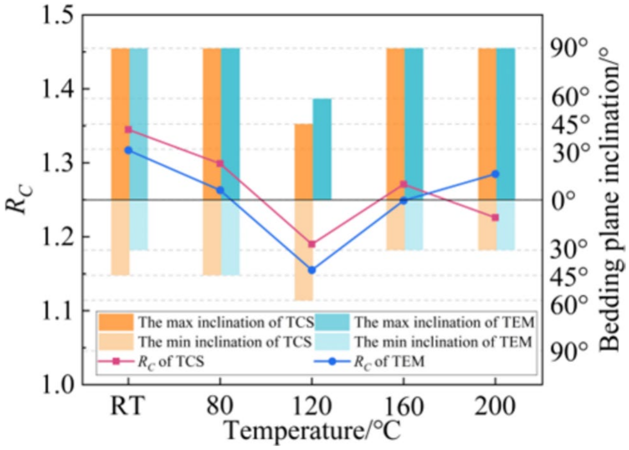

Fig. 20 Evolution of R_C of TCS and TEM with temperature and the maximum and minimum inclinations of TCS and TEM at different temperatures

temperature. The maximum and minimum values exhibit unusual behavior at 120 °C, and $R_{C(\mathrm{TCS})}$ and $R_{C(\mathrm{TEM})}$ show a sharp decrease at 120 °C, likely due to the dissipation of weakly bound water, as analyzed above.

Stress-induced anisotropy occurs under true triaxial loading, distinct from the anisotropy caused by the bedding planes of shale. This type of anisotropy arises from non-hydrostatic pressure (Zhang et al. 2021b). To explore the relationship between bedding plane anisotropy and stress-induced anisotropy, the peak strain ratio $\varepsilon_{\mathrm{p}2}/\varepsilon_{\mathrm{p}3}$ of σ_2 and σ_3 was calculated, and the variation of $\varepsilon_{\mathrm{p}2}/\varepsilon_{\mathrm{p}3}$ with increasing BPI at different temperatures was plotted, as shown in Fig. 21. In non-true triaxial tests, when the angle between the bedding plane and the horizontal plane falls within a certain range, failure tends to occur as shear slip along the bedding plane, resulting in $\varepsilon_{\mathrm{p}2} > \varepsilon_{\mathrm{p}3}$. Under true triaxial loading of isotropic rock, deformation in the σ_3 direction is more pronounced due to inhibition by σ_2, leading to $\varepsilon_{\mathrm{p}2} < \varepsilon_{\mathrm{p}3}$. As shown in Fig. 21a, $\varepsilon_{\mathrm{p}2}/\varepsilon_{\mathrm{p}3}$ shows an upward trend with increasing BPI. When the BPIs are 0° and 30°, $\varepsilon_{\mathrm{p}2}/\varepsilon_{\mathrm{p}3}$ is almost less than 1, indicating that shale samples with BPIs of 0° and 30° are dominated by stress-induced anisotropy. When the BPI is 45°, $\varepsilon_{\mathrm{p}2}/\varepsilon_{\mathrm{p}3}$ is larger at 200 °C and smaller at 160 °C, with values around 0.75 at other temperatures. Temperature affects the cohesion of the bedding plane, causing the fracture plane at 160 °C and 200 °C to be parallel to σ_3. However, fractures appear on surfaces loaded with σ_2 and σ_3 at 160 °C (Fig. 21b), and temperature completely aligns the fracture direction with σ_3 at 200 °C (Fig. 21b). Thus, at 160 °C, stress-induced anisotropy dominates, while at 200 °C, bedding plane anisotropy dominates. At other temperatures, shale samples with a BPI of 45° show true triaxial failure forms and are more affected by stress-induced anisotropy. When the BPI is 60°, shale samples with a BPI of 60° exhibit shear failure along the bedding plane at all temperatures, so $\varepsilon_{\mathrm{p}2}/\varepsilon_{\mathrm{p}3}$ is generally greater than 1, indicating that bedding plane anisotropy is stronger than stress-induced anisotropy. When the BPI is 90°, $\varepsilon_{\mathrm{p}2}/\varepsilon_{\mathrm{p}3}$ is greater than 1 at all temperatures, indicating dominance by bedding plane anisotropy. However, the bedding plane of shale samples with a BPI of 90° is perpendicular to σ_2, and the failure forms suggest no possibility of shear slip in the σ_2 direction, which is puzzling.

Therefore, to analyze the deformation characteristics of shale samples with a BPI of 90°, an additional true triaxial

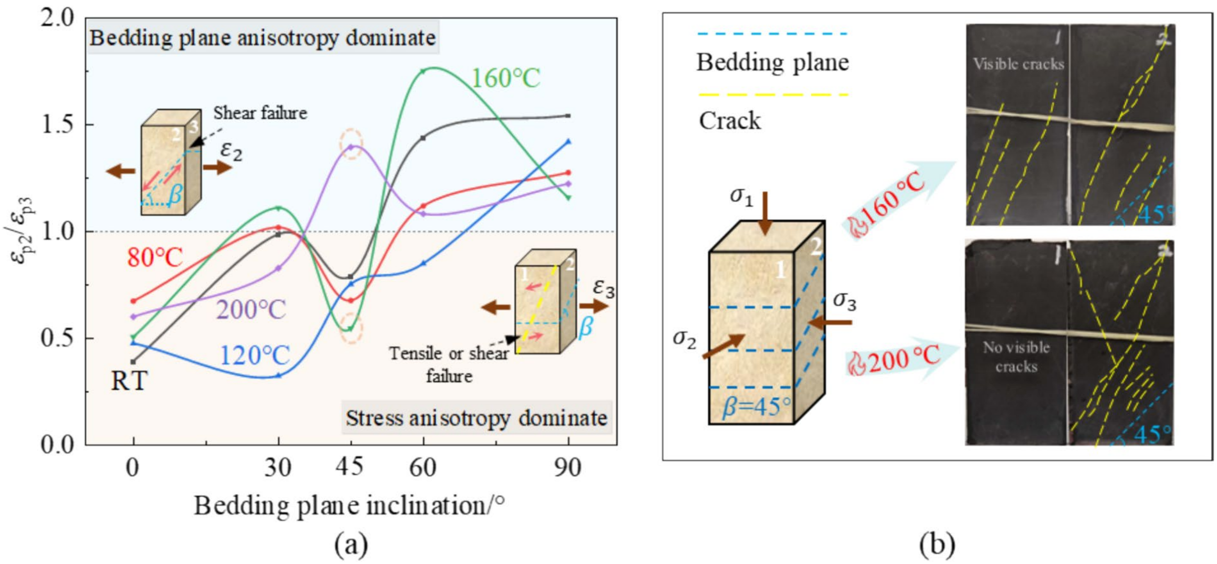

(a)

(b)

Fig. 21 Evolution of $\varepsilon_{\mathrm{p}2}/\varepsilon_{\mathrm{p}3}$ with BPI at different temperatures (**a**) and failure morphologies of shales with a BPI of 45°at 160 ℃ and 200 ℃ (**b**)

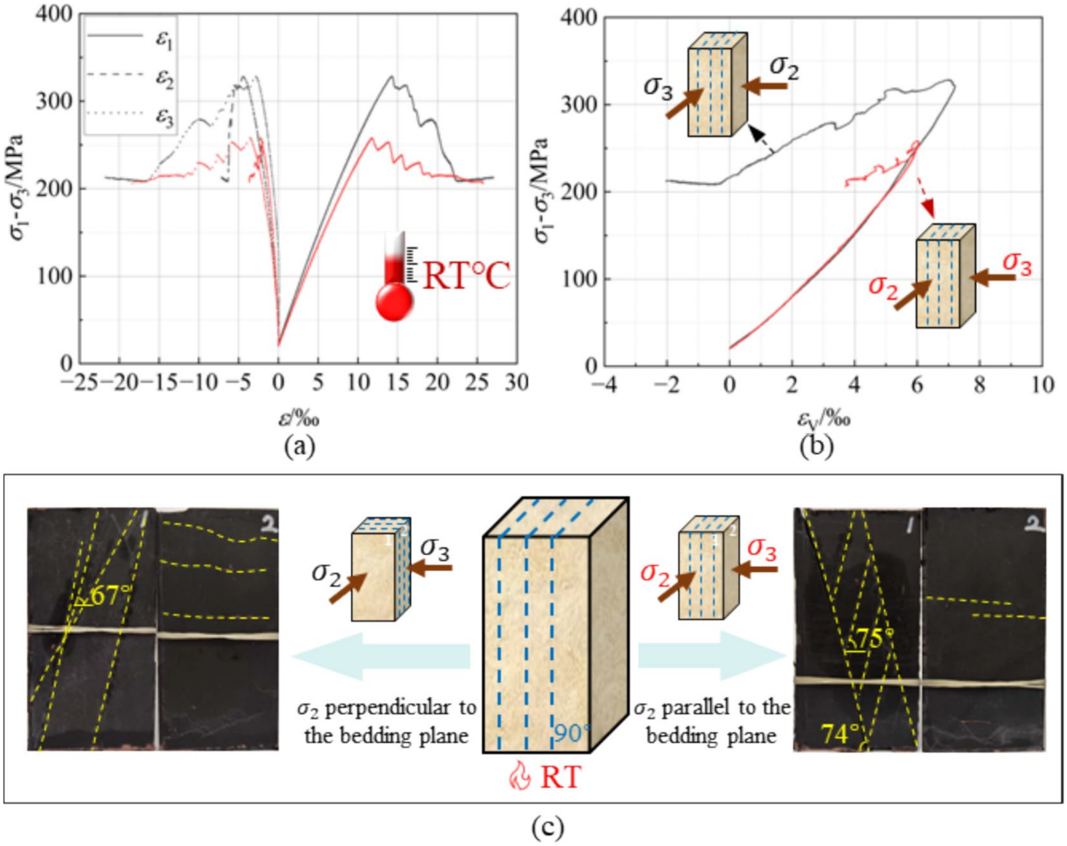

Fig. 22 Stress–strain curves of shales with different relative positions of σ_2 loading direction and strike of 90° bedding planes at RT (**a**) and (**b**) and their failure morphologies (**c**)

compression test was conducted on a shale sample with a BPI of 90° at room temperature (RT). σ_2 and σ_3 were still set at 80 MPa and 60 MPa, but the loading direction was opposite to that in Fig. 2c. That is, σ_2 was set parallel to the strike of the bedding plane of 90°. Figure 22 shows the stress–strain curves and failure forms of two shale samples with a BPI of 90° at RT. The black line in the stress–strain curves represents the strike of the bedding plane parallel to σ_3, and the red line represents the strike of the bedding plane parallel to σ_2. As seen in Fig. 22a, the TCS of the shale sample with the bedding plane parallel to σ_2 is significantly lower than that of the shale sample with the bedding plane parallel to σ_3. Stress drops occur after the peak in both samples, with more frequent drops in the sample with the bedding plane parallel to σ_2, while the drops are larger in the sample with the bedding plane parallel to σ_3. In Fig. 22b, the volumetric strain curves of both samples coincide before the peak. However, at residual stress, the volume expansion of the sample with the bedding plane parallel to σ_3 is greater than that of the sample with the bedding plane parallel to σ_2. Figure 22c shows that when the bedding plane is parallel to σ_2, the fracture planes remain parallel to σ_2, displaying a true triaxial failure form. Two fractures of 74° run through the top and bottom of the sample, with several nearly parallel fracture groups at 75° connecting the two primary fractures in the middle. This failure form differs from that of the sample with the bedding plane parallel to σ_3. It has larger fracture inclinations and contains parallel fracture groups because the bedding plane influences fracture development during expansion along the σ_3 direction. The

Table 7 True triaxial compression experimental data of shale samples with a BPI of 90°

σ_2 loading direction	σ_p/MPa	$\varepsilon_1/10^{-3}$	$\varepsilon_2/10^{-3}$	$\varepsilon_3/10^{-3}$	σ_r/MPa	$\varepsilon_r/10^{-3}$	E/GPa	B_4	B_5
Vertical to bedding plane	328.40	14.29	– 4.42	– 2.87	208.72	22.76	24.16	0.364	0.042
Parallel to bedding plane	258.15	11.74	– 2.19	– 3.52	215.03	19.65	22.76	0.167	0.012

calculated mechanical parameters of the two shale samples are shown in Table 7. The $\varepsilon_{p2}/\varepsilon_{p3}$ ratio for the sample with the bedding plane parallel to σ_2 is 0.623, indicating smaller deformation in the σ_2 direction than in the σ_3 direction. This is due to the bedding planes being separated during expansion. The $\varepsilon_{p2}/\varepsilon_{p3}$ ratio for the sample with the bedding plane parallel to σ_3 is 1.543, indicating greater deformation in the σ_2 direction than in the σ_3 direction. This could be attributed to the low stiffness of the bedding plane (Geng et al. 2016), resulting in severe deformation under compression. The calculated B_4 and B_5 values for the shale sample with the bedding plane parallel to σ_3 are 0.364 and 0.042, respectively. For the sample with the bedding plane parallel to σ_2, they are 0.167 and 0.012. This indicates that when the bedding plane is parallel to σ_2, brittleness decreases significantly. The weak bedding plane perpendicular to the expansion direction of σ_3 consumes part of the energy in tension or shear slip during the failure process, preventing severe energy release. Conversely, when the bedding plane is parallel to σ_3, shear slip occurs in the high-strength shale matrix, releasing intense energy and resulting in greater brittleness. In summary, the relative direction of the true triaxial principal stress loading direction and the bedding plane strike affects the failure forms, brittleness, and anisotropy of shale.

5.3 Potential Engineering Applications

In the process of deep shale gas exploitation, reservoirs are typically found in high-temperature formations with a significant horizontal stress difference. Higher brittleness in the reservoir rock increases the likelihood of forming a complex fracture network, thereby enhancing the permeability of shale and improving shale gas output. The test results in this paper demonstrate that Bedding Plane Inclination (BPI), temperature, and stress loading direction significantly impact shale brittleness. Therefore, it is essential to consider these factors comprehensively in shale gas exploitation projects to increase deep shale gas production. At high temperatures, the shear strength of the bedding plane decreases. If hydraulic fracturing operations are conducted in high-temperature regions and the angle between the bedding plane and the σ_3 direction is near 60°, the likelihood of fracturing fluid flowing into fractures parallel to the bedding plane increases. This can result in the dispersion of water pressure energy, which may hinder the expansion of hydraulic fractures in the shale matrix. Due to limitations in detection technology, it may be challenging to accurately and simply obtain the real-time temperature at various positions within the reservoir, necessitating further technological development. After injecting normal-temperature fracturing fluid into a high-temperature reservoir, the cooling effect will further alter the physical and mechanical properties of shale, which also needs to be considered. Additionally, significant brittleness changes occur with varying BPI. In this test, when the angle between the bedding plane and the horizontal plane is 90°, and the bedding plane is parallel to the σ_3 direction, the brittleness is at its maximum. The resulting cracks are dense and evenly distributed, aligning with the goal of achieving a complex fracture network. Therefore, in shale gas exploitation, it is crucial to consider the relationship between the angle of perforation clusters, BPI, and the direction of in situ stress. By rationally arranging the distribution of BPI and in situ stress, the maximum brittleness of shale can be achieved, enhancing the complexity of the fracture network and increasing shale gas production.

6 Conclusions

In this paper, a series of true triaxial tests were conducted on anisotropic shale samples at real-time temperatures (RT-200℃) to investigate the mechanical properties and failure characteristics of shale in deep shale gas reservoirs under high temperatures and high horizontal in situ stress differences. The study analyzed the variation of strength, deformation, failure mode, and brittleness of shale samples with temperature under true triaxial loading. The anisotropy of the mechanical properties of shale in a deep shale gas environment was also explored. The main conclusions are summarized as follows:

1. During the heating process from RT to 200℃, both physical and numerical tests showed that the reduction in TCS is primarily caused by thermal damage before approximately 120℃. Physical tests revealed that the TCS and TEM of shale exhibit obvious temperature thresholds after 120℃, which correspond to the dissipation temperature intervals of adsorbed water in clay minerals within shale. In contrast, numerical simulation tests without considering hydraulic coupling showed no obvious temperature thresholds for TCS and TEM. This suggests that the changes in mechanical properties of shale with temperature are likely caused by variations in internal water content.
2. The failure mode of shale under true triaxial loading in physical tests is determined by temperature and BPI. At BPIs of 0°, 30°, and 90°, the failure mode is shear failure with the fracture plane parallel to σ_2. At a BPI of 60°, shear failure occurs along the bedding plane at all temperatures. At a BPI of 45°, shear failure occurs with the fracture plane parallel to σ_2 at RT, 80℃, and 120℃, but parallel to σ_3 at 160℃ and 200℃. Numerical simulation results indicate that the change in failure mode at high temperatures is caused by the difference in thermal expansion coefficients between the bedding plane and the matrix. According to analysis of Coulomb's law, the

change in failure mode for shale samples with BPIs of 45° and 60° is due to the weakening of the cohesion of the bedding plane by temperature, which is consistent with the numerical simulation results.

3. Brittleness indices based on stress–strain curve parameters were used to evaluate the brittleness of anisotropic shale samples at different temperatures. Correlation analysis shows that results based on the same type of parameters are consistent. Brittleness indices based on stress drop and velocity of stress drop post-peak best match post-peak phenomena, such as sound during failure, fracture surface characteristics after failure, and failure mode. Brittleness is influenced by both temperature and BPI, with shale samples at a BPI of 90° exhibiting higher brittleness, those at 60° showing lower brittleness, and those at 45° showing reduced brittleness at 160℃ and 200℃.
4. TCS and TEM show significant anisotropy. The most unfavorable angles for most shale samples under true triaxial loading range from 30° to 45°, with maximum values occurring at 90°. The overall trend of $\varepsilon_{p2}/\varepsilon_{p3}$ increases with BPI, indicating that deformation is dominated by stress-induced anisotropy at low BPI and by the anisotropy of the bedding plane at high BPI. The relative orientation of the loading direction of true triaxial stress and the bedding plane significantly affects the mechanical properties and failure characteristics of shale. The TCS, $\varepsilon_{p2}/\varepsilon_{p3}$, and brittleness of σ_2 parallel to a bedding plane of 90° at RT are significantly smaller than those of σ_2 perpendicular to a bedding plane of 90°, and the failure forms are notably different.

Funding Open access funding provided by The Hong Kong Polytechnic University. This study was funded by the National Natural Science Foundation of China (Grant Nos. 42377156, 42,077,251). This research was also financially supported by the Hong Kong Polytechnic University Strategic Importance Fund (ZE2T) and the Project of Research Institute of Land and Space (CD78).

Data Availability All data generated or analyzed during this study are available.

Declarations

Conflict of interest The authors declared that they have no conflicts of interest in this work.

References

Andreev G (1995) Brittle failure of rock material: test results and constitutive models. A. A. Balkema, Rotterdam, p 446

Chen M, Jin Y (2012) Optimization of shale gas fracturing process parameters based on core analysis. Pet Drill Tech 40(4):7–12. https://doi.org/10.3969/j.issn.1001-0890.2012.04.002. (**in Chinese**)

Chen G, Jiang W, Sun X et al (2019) Quantitative evaluation of rock brittleness based on crack initiation stress and complete stress–strain curves. Bull Eng Geol Environ 78:5919–5936. https://doi.org/10.1007/s10064-019-01486-2

Chen B, Li Y, Tang C (2024) Numerical study on the zonal disintegration of a deeply buried high-temperature roadway during cooling. Comput Geotech 165:105848. https://doi.org/10.1016/j.compgeo.2023.105848

Cheng J, Wan Z, Zhang Y et al (2015) Experimental study on anisotropic strength and deformation behavior of a coal measure shale under room dried and water saturated conditions. Shock Vib 2015:1–13. https://doi.org/10.1155/2015/290293

Cook N (1967) Rock mechanics and the design of structures in rock: by Leonard Obert and Wilbur I. J Franklin Inst 284(5):335. https://doi.org/10.1016/0016-0032(67)90559-5

Fairhurst C, Hudson J (1999) Draft ISRM suggested method for the complete stress–strain curve for intact rock in uniaxial compression. Int J Rock Mech Min Sci 36(3):279–289. https://doi.org/10.1016/S0148-9062(99)00006-6

Fang J, Song J, Li X (2021) Quantitative analysis of clay minerals' influence on bound water characteristics and mechanical properties of soft soils. J Eng Geol 29(05):1303–1311. https://doi.org/10.13544/j.cnki.jeg.2021-0327

Feng D, Li X, Wang X et al (2018) Water adsorption and its impact on the pore structure characteristics of shale clay. Appl Clay Sci 155:126–138. https://doi.org/10.1016/j.clay.2018.01.017

Feng X, Gong B, Cheng X et al (2022) Anisotropy and microcrack-induced failure precursor of shales under dynamic splitting. Geomat Nat Haz Risk 13(1):2864–2889. https://doi.org/10.1080/19475705.2022.2137440

Geng Z, Chen M, Jin Y et al (2016) Experimental study of brittleness anisotropy of shale in triaxial compression. J Nat Gas Sci Eng 36:510–518. https://doi.org/10.1016/j.jngse.2016.10.059

Goktan R, Yilmaz N (2005) A new methodology for the analysis of the relationship between rock brittleness index and drag pick cutting efficiency. Int J South Afr Inst Min Metall 105(10):727–733

Guo Y, Huang L, Li X et al (2020) Experimental investigation on the effects of thermal treatment on the physical and mechanical properties of shale. J Nat Gas Sci Eng 82:103496. https://doi.org/10.1016/j.jngse.2020.103496

Guo P, Li X, Yang W et al (2022a) Experimental study on hydrofracture propagation through perforated wellbore in naturally fractured Guanyinqiao calcareous mudstone under true triaxial stress. J Nat Gas Sci Eng 99:104415. https://doi.org/10.1016/j.jngse.2022.104415

Guo Y, Li X, Huang L (2022b) Changes in thermophysical and thermomechanical properties of thermally treated anisotropic shale after water cooling. Fuel 327:125241. https://doi.org/10.1016/j.fuel.2022.125241

Guo Y, Wang D, Han X et al (2022c) Evaluation of fracturability of shale reservoirs in the longmaxi formation in southern sichuan basin. Front Earth Sci 10:993829. https://doi.org/10.3389/feart.2022.993829

Guo W, Guo Y, Cai Z et al (2023) Mechanical behavior and constitutive model of shale under real-time high temperature and high stress conditions. J Petrol Explor Prod Technol 13:827–841. https://doi.org/10.1007/s13202-022-01580-4

Han L, Li X, Liu Z et al (2023) Study on rock mechanics characteristics of deep shale in Luzhou block and the influence on reservoir fracturing. Energy Sci Eng 11:4–21. https://doi.org/10.1002/ese3.1360

Huang L, Guo Y, Li X (2022) Failure characteristics of shale after being subjected to high temperatures under uniaxial compression. Bull Eng Geol Environ 81:33. https://doi.org/10.1007/s10064-021-02492-z

Hucka V, Das B (1974) Brittleness determination of rocks by different methods. Int J Rock Mech Min Sci Geomech Abstr 11(10):389–392. https://doi.org/10.1016/0148-9062(74)91109-7

Jager C (1979) Rock mechanics and engineering. Cambridge University Press, Cambridge

Li LC, Tang CA, Li G et al (2012a) Numerical simulation of 3D hydraulic fracturing based on an improved flow-stress-damage model and a parallel FEM technique. Rock Mech Rock Eng 45(5):801–818. https://doi.org/10.1007/s00603-012-0252-z

Li Y, Wang X, Wang J (2012b) Cation exchange, interlayer spacing, and thermal analysis of Na/Ca-montmorillonite modified with alkaline and alkaline earth metal ions. J Therm Anal Calorim 110:1199–1206. https://doi.org/10.1007/s10973-011-2109-1

Liu X, Ma X, He M et al (2023) Experimental investigation on anisotropy of rocks using digital drilling technology. Sustainability-Basel 15:13357. https://doi.org/10.3390/su151813357

Lu H, Xie H, Luo Y et al (2021) Failure characterization of Longmaxi shale under direct shear mode loadings. Int J Rock Mech Min Sci 148:104936. https://doi.org/10.1016/j.ijrmms.2021.104936

Ma X, Xie J, Yong R et al (2020) Geological characteristics and high production control factors of shale gas reservoirs in Silurian Longmaxi Formation, southern Sichuan Basin. SW China Petrol Explor Dev 47(5):901–915. https://doi.org/10.1016/S1876-3804(20)60105-7

Ma X, Dong W, Hu D et al (2023) Mechanical properties of granite at high temperature subjected to true triaxial compression. Int J Rock Mech Min Sci 164:105313. https://doi.org/10.1016/j.ijrmms.2022.105313

Masri M, Sibai M, Shao J et al (2014) Experimental investigation of the effect of temperature on the mechanical behavior of Tournemire shale. Int J Rock Mech Min Sci 70:185–191. https://doi.org/10.1016/j.ijrmms.2014.05.007

Meng F, Zhou H, Zhang C et al (2015) Evaluation methodology of brittleness of rock based on post-peak stress–Strain curves. Rock Mech Rock Eng 48(5):1787–1805. https://doi.org/10.1007/s00603-014-0694-6

Meng M, Chen P, Ren R (2019) Statistic evaluation of failure criteria in wellbore stability with temperature effects. Fuel 252:730–752. https://doi.org/10.1016/j.fuel.2019.04.110

Nie H, Jin Z, Li P et al (2023) Deep shale gas in the Ordovician–Silurian Wufeng–Longmaxi formations of the Sichuan Basin, SW China: insights from reservoir characteristics, preservation conditions and development strategies. J Asian Earth Sci 244:105521. https://doi.org/10.1016/j.jseaes.2022.105521

Qin Y, Xu N, Chen W et al (2023) Experimental study on the effect of high temperature on the physical and mechanical properties of sandstone with different bedding angles. Appl Sc-Basel 13(24):13199. https://doi.org/10.3390/app132413199

Rao Q, Wang Z, Xie H et al (2007) Experimental study of mechanical properties of sandstone at high temperature. J Cent South Univ Technol 14(Suppl 1):478–483. https://doi.org/10.1007/s11771-007-0311-x

Rickman R, Mullen M, Petre J et al (2008) A practical use of shale petrophysics for stimulation design optimization: All shale plays are not clones of the Barnett Shale. In: SPE Annual Technical Conference and Exhibition, Denver, USA. p 115258

Rybacki E, Meier T, Dresen G (2016) What controls the mechanical properties of shale rocks? Part II: brittleness. J Petrol Sci Eng 144:39–58. https://doi.org/10.1016/j.petrol.2016.02.022

Saroglou H, Tsiambaos G (2008) A modified Hoek-Brown failure criterion for anisotropic intact rock. Int J Rock Mech Min Sci 45(2):223–234. https://doi.org/10.1016/j.ijrmms.2007.05.004

Selvadurai APS, Rezaei Niya SM (2020) Effective thermal conductivity of an intact heterogeneous limestone. J Rock Mech Geotech Eng 12(4):682–692. https://doi.org/10.1016/j.jrmge.2020.04.001

Shi Z (2023) Study on pore water distribution and permeability in kaolin consolidation process. Dissertation, GuiLin University of Technology (**in Chinese**)

Sun Q, Zhang W, Xue L et al (2015) Thermal damage pattern and thresholds of granite. Environ Earth Sci 74(3):2341–2349. https://doi.org/10.1007/s12665-015-4234-9

Sydney P (1966) Handbook of physical constants. Geological Society of America, Boulder

Tang CA, Kaiser PK (1998) Numerical simulation of cumulative damage and seismic energy release during brittle rock failure: part I—fundamentals. Int J Rock Mech Min Sci 35(2):113–121. https://doi.org/10.1016/S0148-9062(97)00009-0

Tao W, Tang H, Wang Y et al (2020) Evaluation of methods for determining rock brittleness under compression. J Nat Gas Sci Eng 78:103321. https://doi.org/10.1016/j.jngse.2020.103321

Tarasov B, Potvin Y (2013) Universal criteria for rock brittleness estimation under triaxial compression. Int J Rock Mech Min Sci 59:57–69. https://doi.org/10.1016/j.ijrmms.2012.12.011

Tian H, Kempka T, Xu N et al (2012) Physical properties of sandstones after high temperature treatment. Rock Mech Rock Eng 45:1113–1117. https://doi.org/10.1007/s00603-012-0228-z

Vachaparampil A, Ghassemi A (2017) Failure characteristics of three shales under true-triaxial compression. Int J Rock Mech Min Sci 100:151–159. https://doi.org/10.1016/j.ijrmms.2017.10.018

Wang H (2021) Research on the evolution mechanism and numerical simulation of thermally induced microcracks in shale. Dissertation, Xi'an Shiyou University (**in Chinese**)

Wang Q, Xiong H (2002) Quantitative analysis and hydration mechanism of clay surface bound water. Petroleum industry press, Beijing (**in Chinese**)

Wang M, Lun Z, Zhao C et al (2020a) Influences of primary moisture on methane adsorption within lower Silurian Longmaxi shales in the Sichuan Basin, China. Energ Fuel 34:10810–10824. https://doi.org/10.1021/acs.energyfuels.0c01932

Wang S, Zhao W, Fu X et al (2020b) A universal method for quantitatively evaluating rock brittle-ductile transition behaviors. J Petrol Sci Eng 195:107774. https://doi.org/10.1016/j.petrol.2020.107774

Wang G, Yang D, Liu S et al (2021) Experimental study on the anisotropic mechanical properties of oil shales under real-time high-temperature conditions. Rock Mech Rock Eng 54(12):6565–6583. https://doi.org/10.1007/s00603-021-02624-7

Wang H, Ma T, Liu Y et al (2023) Numerical and experimental investigation of the anisotropic tensile behavior of layered rocks in 3D space under Brazilian test conditions. Int J Rock Mech Min Sci 170:105558. https://doi.org/10.1016/j.ijrmms.2023.105558

Wawersik WR, Fairhurst C (1970) A study of brittle rock fracture in laboratory compression experiments. Int J Rock Mech Min Sci Geotech Abstr 7(5):561–575. https://doi.org/10.1016/0148-9062(70)90007-0

Wei P, Zhou S, Zheng Y et al (2024) Nanoscale stick-slip behavior and hydration of hydrated illite clay. Comput Geotech 166:105976. https://doi.org/10.1016/j.compgeo.2023.105976

Xia Y, Li L, Tang C et al (2017) A new method to evaluate rock mass brittleness based on stress–strain curves of class I. Rock Mech Rock Eng 50(5):1123–1139. https://doi.org/10.1007/s00603-017-1174-6

Xia Y, Zhou H, Zhang C et al (2019) The evaluation of rock brittleness and its application: a review study. Eur J Environ Civ En 26(1):239–279. https://doi.org/10.1080/19648189.2019.1655485

Yang S, Xu P, Li Y et al (2017) Experimental investigation on triaxial mechanical and permeability behavior of sandstone after exposure to different high temperature treatments. Geothermics 69:93–109. https://doi.org/10.1016/j.geothermics.2017.04.009

Yang S, Yin P, Huang Y et al (2019) Strength, deformability and X-ray micro-CT observations of transversely isotropic composite rock under different confining pressures. Eng Fract Mech 214:1–20. https://doi.org/10.1016/j.engfracmech.2019.04.030

Yin P (2020) Study on mechanical behavior and hydraulic fracturing mechanism of Longmaxi formation shale in Southern Sichuan Basin. Dissertation, China University of Mining and Technology (**in Chinese**)

Yu W (2015) Analysis and numerical simulation of influencing factors of shale thermal conductivity. Dissertation, SouthWest Petroleum University (**in Chinese**)

Zhang Q, Fan X, Chen P et al (2020) Geomechanical behaviors of shale after water absorption considering the combined effect of anisotropy and hydration. Eng Geol 269:105547. https://doi.org/10.1016/j.enggeo.2020.105547

Zhang Q, Yao B, Fan X et al (2021a) A modified Hoek–Brown failure criterion for unsaturated intact shale considering the effects of anisotropy and hydration. Eng Fract Mech 241:107369. https://doi.org/10.1016/j.engfracmech.2020.107369

Zhang Y, Feng X, Yang C et al (2021b) Evaluation method of rock brittleness under true triaxial stress states based on pre-peak deformation characteristic and post-peak energy evolution. Rock Mech Rock Eng 54(3):1277–1291. https://doi.org/10.1007/s00603-020-02330-w

Zhang Y, Zhao Y, Long A et al (2024) Combined effects of bedding anisotropy and matrix heterogeneity on hydraulic fracturing of shales from Changning and Lushan, South China: an experimental investigation. J Asian Earth Sci 259:105908. https://doi.org/10.1016/j.jseaes.2023.105908

Zhao D, Xia Y, Zhang C et al (2022a) Failure modes and excavation stability of large-scale columnar jointed rock masses containing interlayer shear weakness zones. Int J Rock Mech Min Sci 159:105222. https://doi.org/10.1016/j.ijrmms.2022.105222

Zhao D, Xia Y, Zhang C et al (2022b) Laboratory test and numerical simulations for 3D printed irregular columnar jointed rock masses under biaxial compression. Bull Eng Geol Environ 81:124. https://doi.org/10.1007/s10064-022-02626-x

Zhao C, Liu J, Lyu C et al (2023a) Mechanical responses and failure characteristics of Longmaxi formation shale under real-time high temperature and high-stress coupling. Eng Fail Anal 152:107490. https://doi.org/10.1016/j.engfailanal.2023.107490

Zhao D, Xia Y, Zhang C et al (2023b) A new method to investigate the size effect and anisotropy of mechanical properties of columnar jointed rock mass. Rock Mech Rock Eng 56(4):2829–2859. https://doi.org/10.1007/s00603-022-03200-3

Zhao G, Guo Y, Yang C et al (2023c) Anisotropic mechanical behavior of ultra-deep shale under high in-situ stress, a case study in the Luzhou block of the southern Sichuan Basin, China. Int J Rock Mech Min Sci 170:105536. https://doi.org/10.1016/j.ijrmms.2023.105536

Zhao G, Guo Y, Wang L et al (2024) Experimental study on mechanical, brittleness, and fracture behavior of deep shales subjected to fracturing fluid-shale interactions at reservoir temperature and in-situ stress conditions. Rock Mech Rock Eng 57:27–44. https://doi.org/10.1007/s00603-023-03555-1

Zheng Z, Zheng H, Zhao J et al (2023) Ductile–brittle quantitative evaluation of rock based on post-peak properties under true triaxial stress. Geomech Geophys Geo 9:81. https://doi.org/10.1007/s40948-023-00567-7

Zhou J, Ma S (2024) SPSSAU research data analysis methods and applications. Publishing House of Electronics Industry, Beijing

Zhou Q, Zhu Z, Liu W et al (2024) Hydraulic fracturing behaviors of shale under coupled stress and temperature conditions simulating different burial depths. Int J Min Sci Techno 34(6):783–797. https://doi.org/10.1016/j.ijmst.2024.06.005

Zhu Z, Li J, Lin F et al (2020) Experimental research on desorption curves of soil samples under different mineral compositions. Chin J Geotech Eng 42(01):175–180. https://doi.org/10.11779/CJGE202001020. (**in Chinese**)

Zou C, Yang Z, Dai J et al (2015) The characteristics and significance of conventional and unconventional Sinian-Silurian gas systems in the Sichuan Basin, central China. Mar Pet Geol 64:386–402. https://doi.org/10.1016/j.marpetgeo.2015.03.005